



저작자표시-비영리-변경금지 2.0 대한민국

이용자는 아래의 조건을 따르는 경우에 한하여 자유롭게

- 이 저작물을 복제, 배포, 전송, 전시, 공연 및 방송할 수 있습니다.

다음과 같은 조건을 따라야 합니다:



저작자표시. 귀하는 원저작자를 표시하여야 합니다.



비영리. 귀하는 이 저작물을 영리 목적으로 이용할 수 없습니다.



변경금지. 귀하는 이 저작물을 개작, 변형 또는 가공할 수 없습니다.

- 귀하는, 이 저작물의 재이용이나 배포의 경우, 이 저작물에 적용된 이용허락조건을 명확하게 나타내어야 합니다.
- 저작권자로부터 별도의 허가를 받으면 이러한 조건들은 적용되지 않습니다.

저작권법에 따른 이용자의 권리는 위의 내용에 의하여 영향을 받지 않습니다.

이것은 [이용허락규약\(Legal Code\)](#)을 이해하기 쉽게 요약한 것입니다.

[Disclaimer](#)

Thesis for the Degree of Master of Engineering

Study on Cell Efficiency Change by Carbon Nanofiber in
Silver Paste for Front side Metallization of Crystalline
Silicon Solar Cells with Dispensing Printing

By

Chonticha Kunpai

Department of Graphic Arts Engineering

Pukyong National University

August, 2016

Study on Cell Efficiency Change by Carbon Nanofiber in Silver Paste for Front side Metallization of Crystalline Silicon Solar Cells with Dispensing Printing

(결정질 실리콘 태양전지 전면전극의 디스펜싱 인쇄용 실버 페이스트에서
카본 나노파이버 첨가가 셀효율에 미치는 영향에 대한 연구)

Advisor: Prof. Dong Youn Shin

by

Chonticha Kunpai

A thesis submitted in partial fulfillment of the requirements
for the degree of

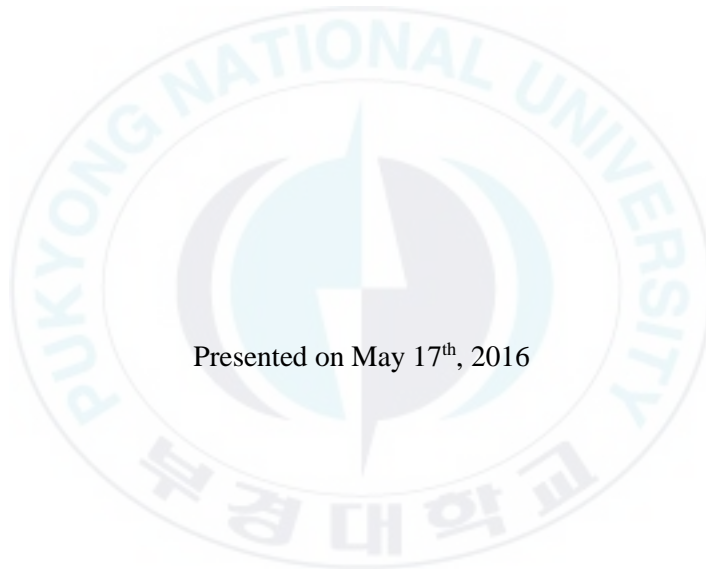
Master of Engineering

in Department of Graphic Arts Engineering, The Graduate School,
Pukyong National University

August 2016

Pukyong National University

As members of the Dissertation Committee, we certify that we recommended this dissertation prepared by Chonticha Kunpai, titled “*Study on Cell Efficiency Change by Carbon Nanofiber in Silver Paste for Front side Metallization of Crystalline Silicon Solar Cells with Dispensing Printing*” be accepted as fulfilling the dissertation requirement for the Master’s degree of Engineering.



Presented on May 17th, 2016

Approved:

Dissertation Committee Chair: Ka-Hyun Kim (PhD) Signature: _____

Dissertation Committee: Hee-Eun Song (PhD) Signature: _____

Dissertation Committee: Dong-Youn Shin (PhD) Signature: _____

Acknowledgements

Firstly, I would like to express my sincere gratitude to my supervisor Prof. Dong-Youn Shin for the continuous support of my study and related research, for his patience, motivation, and immense knowledge. His guidance helped me in all the time of research and writing of this dissertation. Without his guidance and persistence help, this dissertation would not have been possible.

Besides my supervisor, I would like to thank the rest of my thesis committee: Dr. Ka-Hyun Kim and Dr. Hee-Eun Song from Korean Institute Energy Research for their insightful comments and encouragement.

This dissertation would not have been possible without funding from the Basic Science Research Program through the National Research Foundation of Korea (NRF), the Ministry of Education, Science and Technology (Grant No. 2012R1A1A2038889), and the Research and Development Program of the Korea Institute of Energy Research (Grant No. B5-2420).

Finally, I would like to thank my family for supporting me spiritually throughout writing this dissertation and my life in general.

Chonticha Kunpai

August, 2016

Contents

Chapter	Page
Contents	i
List of tables	iii
List of Figures	iv
Abstract	vii
1. Introduction	1
2. Review of related literature	2
2.1 Solar cells fabrication technology	3
2.1.1 Photolithography	3
2.1.2 Coextrusion printing	4
2.1.3 Screen printing	5
2.1.4 Ink-jet printing	6
2.1.5 Aerosol jet printing	8
2.1.6 Dispensing printing	10
2.2 Carbon nanofiber (CNF)	11
2.2.1 Synthesis and structure of CNF	12
3. Experimental	14
3.1 Characterization of CNF	14
3.1.1 Microstructure characterization of CNF by Transmission Electron Microscope (TEM)	14
3.1.2 Thermo gravimetric analysis (TGA) of CNF	14
3.2 Preparation of silver paste	15
3.2.1 The preparation of in-house developed silver paste	15
3.2.1.1 Carrier vehicle preparation	15
3.2.1.2 Glass frit preparation	16
3.2.1.3 In-house silver paste preparation	18
3.2.2 The preparation of commercially available silver paste containing CNF	20
3.3 Fabrication of crystalline silicon solar cells	21
3.4 Electrical characterization	24
3.4.1 Contact resistivity	24
3.4.2 Resistivity	26
3.5 Morphological characterization	27
3.5.1 Scanning Electron microscope (SEM)	27
3.5.2 Field Emission-Scanning Electron Microscopy (FE-SEM)	27
3.6 Rheological characterization	28
3.7 Solar cell efficiency	28

Contents

Chapter	Page
4. Results and discussion	29
4.1 Microstructure of CNF	29
4.2 The effect of CNF on rheology of silver paste	30
4.3 The effect of CNF on silver paste consumption	32
4.4 The effect of CNF on elongational property and finger line width	33
4.5 The effect of CNF on thermal property	39
4.6 The effect of CNF on electrical properties	40
4.6.1 The effect of CNF on contact resistivity	41
4.6.2 The effect of CNF on resistivity	45
4.7 The effect of CNF on cell efficiency	46
5. Conclusion	49
Appendices	50
Appendix A: Viscosity measurement	51
Appendix B: Contact formation	54
Appendix C: Resistivity measurement on thin rectangular slice	57
Appendix D: Solar cell efficiency	59
Appendix E: Sheet resistance, shunt resistance and I-V curve	61
6. Reference	65

List of tables

Table	Page
1. Comparison price and length of nanofiber	11
2. Three different composition of carrier vehicle	16
3. The composition of glass frit suspension	18
4. Silver paste composition	18
5. Printing condition	37
6. The comparison between average cell efficiency of solar cells fabricated by commercially available silver paste without CNF and commercially available silver paste with 0.2 wt% CNF at ramp-up rate of 100°C/s	46
 Appendices	
A-1 The categorized of viscosity behavior	53
C-1 Size correction factor (C1) of Four-Point Probe Resistivity Measurement on thin, rectangular slice	58
C-2 thickness correction factor (C ₂)	58
D-1 Cell efficiency of commercially available silver paste without CNF	59
D-2 Cell efficiency of commercially available silver paste containing 0.2 wt% CNF	60
E-1 Summary of shunt resistance from I-V curves	62

List of Figures

Figure	Page
1. Predicted trend for finger width	2
2. The pattern generated from positive and negative resist	3
3. The component of coextrusion paste and mechanism principle of the coextrusion printing for front side metallization	4
4. Screen printing method	5
5. Cross section, top view of finger electrode by screen printing and 3D profile of single and d) double screen printing finger electrode	5
6. Schematic diagram of continuous ink-jet (CIJ) printer	6
7. Schematic model of piezoelectric ink-jet printing	7
8. Schematic model of ultrasonic atomizer principle	8
9. Schematic model of pneumatic atomizer principle	8
10. Metallization by aerosol printing	9
11. The adaptation of paste rheology with difference yield stress and young modulus from paste A to C	10
12. SEM image of the rheology development silver paste which dispensed through 40 μm nozzle diameter and parallel 10-nozzle dispensing unit during cell fabrication	11
13. The stacked-cup of CNF structure formation	12
14. Carrier vehicle process chart	15
15. Planetary Micro Mill PULVERISETTE 7 premium line and theory of grinding	16
16. Process chart to make concentrate glass frit	17
17. The silver paste with glass frit pulverization	19
18. The process flow of commercially available silver paste containing CNF	20
19. Thinky mixer (Thinky, ARE-310, Japan) and 3 roll mill (EXAKT Technologies, Inc., EXAKT-50, USA)	20
20. Fabrication of crystalline silicon solar cell process chart	21
21. RTP (AccuThermo AW 610, Allwin21 Corp., USA)	22
22. Zoom stereo microscope	23
23. Total resistance components	24
24. TLM measurement and evaluation of the contact and sheet resistances for TLM measurement	25
25. Arrangement of a 4-point probe on a rectangular sample	26
26. Four point probe and sourcemeter using for measuring the resistivity	27
27. HAAKE MARS 60 Rheometer using for rheological characterization	28
28. TEM image of as-received CNF	29
29. Shear viscosities of silver paste at different CNF concentration	30
30. Yield stress of silver paste containing 0, 0.2, 0.4 and 0.6 wt% CNF	31
31. The influence of CNF on silver paste consumption	32
32. The elongational property of In-house developed silver paste without, with 0.2 wt% CNF and with 0.5 wt% CNF	33

List of Figures

Figure	Page
33. The yield of continuous line at screw pumping of 30, 40, 50, 60 and 70rpm, dispensed commercially available silver paste without CNF at the screw pumping of 30, 40 and 50rpm and dispensed commercially available silver paste containing 0.2 wt% CNF at screw pumping of 30rpm, 40 and 50rpm	34
34. The rheological behavior of the shear thinning silver paste with the recovery of yield stress by dispensing printing The effect of finger line width on screw pumping rpm	35
35. The effect of CNF concentration on finger line width by dispensed on mono-crystalline silicon solar cell and SEM image of dispensed finger electrode at and 0.6 wt% CNF through 75 μm nozzle in diameter	35
36. The effect of CNF concentration on finger line width by dispensed on Photopaper	36
37. The effect of CNF concentration on finger line width by dispensed on photopaper	38
38. The influence of surface condition of silicon solar cell wafer and photopaper on finger line width	38
39. TGA results of pure CNF, pure GFV2172, commercially available silver paste, GFV2172-CNF (1: 0.15), Ag-GFV2172-CNF (1: 1: 0.15) and mixture of commercially available silver paste – CNF (20: 0.5) in weight ratio	39
40. The temperature profile of a crystalline silicon solar cell in RTP	40
41. The statistical analysis of CNF concentration on contact resistivity	41
42. The mechanism to form contact between silver paste without and with CNF	41
43. Mechanism of filtration of the complete blocking filtration law, the intermediate blocking filtration law and the standard blocking law	42
44. Schematic presentation of pore network model and the effect of CNF on penetrability of glass frit	43
45. FESEM image of pure glass frit and mixture of glass frit to CNF at 1:1 volume ratio (1: 0.15 weight ratio)	43
46. The contact resistivity variation with the screw pumping rpm for the finger electrodes which dispensed through 50 μm nozzle in diameter	44
47. The effect of CNF on resistivity	45
48. The J_{sc} of commercially available silver paste with and without CNF at different peak temperature	47
49. The efficiency of commercially available silver paste with and without CNF at different peak temperature	47

List of Figures

Figure	Page
Appendices	
A-1 The measurement principle of viscometer	51
A-2 Schematics of cone-plate and plate-plate model	52
B-1 Model of thick-film contact after firing.	55
B-2 Cross-section of back contact region	56
C-1 The configuration of rectangular slice for resistivity measurement	57
E-1 The equivalent circuit model	61
E-2 Obtaining values for R_s and R_{sh} from I-V curve	61
E-3 I-V curve of cells prepared by commercially available silver paste without and with 0.2 wt% CNF at peak temperature of 790°C	63
E-4 I-V curve of cells prepared by commercially available silver paste without and with 0.2 wt% CNF at peak temperature of 810°C	63
E-5 I-V curve of cells prepared by commercially available silver paste without and with 0.2 wt% CNF at peak temperature of 830°C	64
E-6 J-V curve of cells prepared by commercially available silver paste without and with 0.2 wt% CNF at peak temperature of 790, 810 and 830°C	64

결정질 실리콘 태양전지 전면전극의 디스펜싱 인쇄용 실버 페이스트에서
카본 나노파이버 첨가가 셀효율에 미치는 영향에 대한 연구

촌티샤 쿤파이

부경대학교 대학원 인쇄공학과

요약

결정질 실리콘 태양전지의 셀 효율을 높이기 위하여 수광면의 전극을 미세하면서도 두껍게 형성함으로써 수광량을 최대화하면서도 파워손실을 최소화할 필요성이 있다. 디스펜싱 인쇄는 공압 혹은 스크류 펌프를 이용하여 고정도의 페이스트를 노즐을 통해 밀어내는 인쇄 방식이며, 한 번의 인쇄만으로 고중량비의 전극을 형성할 수 있기 때문에 차세대 결정질 실리콘 태양전지 전극인쇄 방식으로 주목받고 있다. 그러나, 고정도의 실버 페이스트를 고속으로 인쇄 시 실버 페이스트의 토출이 끊기는 단락현상이 발생하며, 이로 인해 연속적인 전극인쇄가 힘들다는 문제점이 있다. 이와 같은 인쇄 중 단락문제를 해결하기 위하여 본 논문에서는 태양전지용 상용 실버 페이스트에 카본 나노파이버를 다양한 무게비율로 첨가하였으며, 카본 나노파이버의 첨가비율에 따라 디스펜싱 인쇄로 제작된 전극의 물리적, 전기적 특성들이 어떻게 변하는지를 연구하였다. 다양한 실험들을 통해 카본 나노파이버를 첨가할 경우 실버 페이스트의 연신특성이 향상됨을 알 수 있었으며, 연신특성이 향상된 실버 페이스트는 인쇄 중 단락현상이 현저히 감소할 뿐만 아니라 전극 미세화에도 기여를 함을 알 수 있었다. 0.2 wt%의 카본 나노파이버를 실버 페이스트에 혼합한 후 50 μm 직경의 노즐로 디스펜싱하여 전극을 형성하였을 때, 기존 실버 페이스트에 비해 31% 가량 더 미세한 전극을 형성할 수 있었다. 이와 같은 전극 미세화는 수광 면적을 최대화함으로써 소성온도 790, 810 및 830도에서 각각 +0.22, +0.10 및 +0.22%p의 셀효율 증대를 가져옴을 알 수 있었다.

1. Introduction

Nowadays, the increasing of worldwide energy consumption demand is not expected to stop in the nearest time. In 2010 to 2040, the world energy consumption will increase 56% from 524 quadrillion British thermal units (Btu) to 820 quadrillion Btu [1] which reported by the statistic of U.S. Energy Information Administration (EIA). The use of conventional fossil fuels has rapidly increased due to the high demand on energy in the developing countries. However, the increased concentration of CO₂ from conventional fossil fuels leads to the global warming.

Therefore the alternative and sustainable energy source has been considered to maintain our planet. The using of renewable energy such as solar cell, natural gas and wind power is the energy which not releases the CO₂ or any greenhouse effect gas.

Solar energy is one type of renewable energy which is sufficient for our requirement of global energy demands. It indicates that enormous potential sun energy would enough to our energy balance.

Photovoltaic (PV) solar cell is one type of solar energy collectors which can convert incident solar radiation directly into electricity without release CO₂ and greenhouse effect gas. For this reason, PV solar cells are negative environment impact.

There are many techniques for constructing the front size metallization. In order to increase the cell efficiency, the narrow and thick finger electrodes are needed to minimize shading and power losses. As oppose to other technologies, the dispensing printing technique offers high aspect-ratio finger electrode with single-pass printing but the disruption of dispensed silver paste during printing has been a hurdle in the art. To alleviate disruption problem, carbon nanofiber (CNF) is incorporated into the commercially available silver paste and its physical and electrical characteristics are investigated.

The purpose of this study is comparing the silver paste with and without CNF by focusing on the morphological, rheological, elongational electrical property and solar cell efficiency.

The result shows that the increase of CNF in silver paste was negative affected on electrical properties. However the incorporation of 0.2 wt% CNF increased the elongational property, resulting in reduction of finger electrode width. A reduction of printed line width improves the solar cell efficiency due to substantially lower shading losses.

2. Review of related literature

Nowadays, the reduction of finger line width is required to minimize shading loosed. According to the International Technology Roadmap for photovoltaic shows that finger widths between 50-60 μm are currently possible in production process [2]. The reducing finger width increases cell efficiency but a further reduction is affected to the contact resistivity between finger electrode and silicon solar cell wafer.

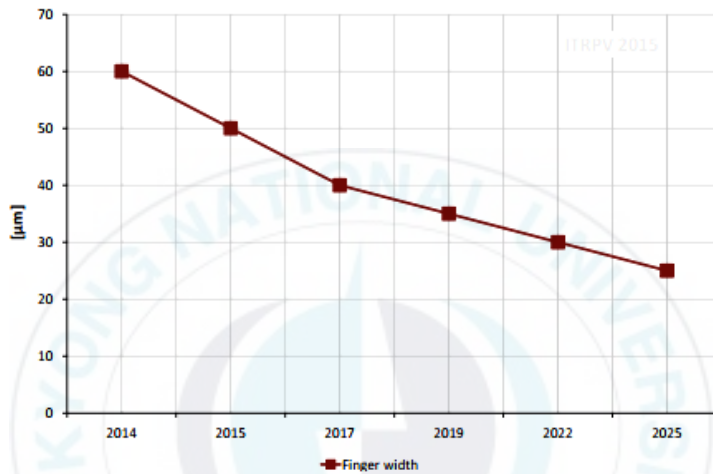


Fig. 1 Predicted trend for finger width [2]

The most important solar cell processing steps is front side metallization for constructing such a narrow finger electrode width, increase the printing quality and cell efficiency. Several techniques are fulfilled in solar cell production to meet these requirements.

2.1 Solar cell fabrication technology

There are many metallization techniques to construct finger electrode such as photolithography, coextrusion, screen printing, ink-jet printing, aerosol printing and dispensing printing.

2.1.1 Photolithography

Photolithography is technique to fabricate high cell efficiency solar cells. The ultrafine and high aspect ratio finger electrode can be constructed by this technique which significantly minimized shading losses and power losses [3, 4]. Therefore, efficiencies of 20.3% of multicrystalline silicon solar cell and 24.7% of mono-crystalline silicon solar cell have been recorded with this technique [5, 6].

There are 2 types of photoresist. The underlying material is removed when the resist is exposed with ultraviolet light, called positive resist. On the contrary, the negative resist remains on the substrate. The pattern differences introduced from the use of negative and positive resist is shown in Fig. 2.

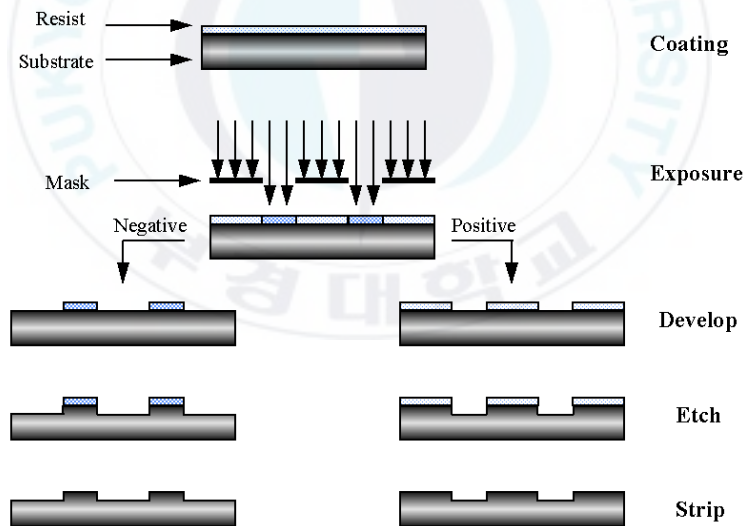


Fig. 2 The pattern generated from positive and negative resist [7]

The basic steps in the lithographic process are shown in Fig. 2. The first step is substrate preparation as cleaning surface. In the next step, a material known as a photoresist which changes the physical or chemical properties upon exposure to radiation is applied by spin coating. After selective mask, the resist coated substrate is then exposed by radiation, typically UV light. Then the unexposed area is removed by wet or dry stripping techniques.

2.1.2 Coextrusion printing

Coextrusion printing is non-contact and mesh mark free metallization technique which can provide narrow finger electrode and strongly enhance the aspect ratio. This technique consists of sacrificial paste and metal paste (Fig. 3a). The printing head and wafer chuck are relatively movement (Fig. 3b). Both metal and sacrificial pastes are extruded out of the nozzle tip on to the solar cell wafer. The spreading out of metal paste which same composition of screen printed paste is prevented by sacrificial paste. The sacrificial paste is removed by solution or heat treatment process after printing.

M. Beutel et al. [8] achieved $23.7\ \mu\text{m}$ finger width with aspect ratio 0.62 on laboratory scale which 21.42% cell efficiency have been recorded by using the coextrusion process.

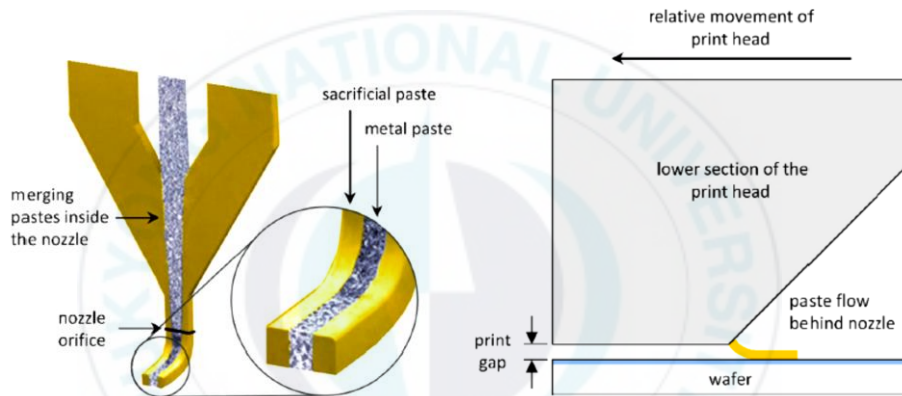


Fig. 3 a) the component of coextrusion paste and b) the mechanism principle of the coextrusion printing for front side metallization [9]

However methods involving costly and complicated equipment as photolithography and coextrusion techniques have difficulties to spread fast. Low cost production and convenient process are required in solar cell industries.

2.1.3 Screen printing

In term of printing, screen printing is a thick-film technology which is expected to be the mainstream for the mass production due to rapid, simple and cost-effective method [10]. First, the screen and wafer are not contacted each other. After putting the paste on screen which consists of stainless steel wires, the pressure is applied to the squeegee for making contact between screen and wafer. Then the squeegee is moved from one side to another side of screen. The silver paste is filled out of the mesh opening and stacked on the wafer. For this technique the finger line width depends on size of mesh opening. The screen printing principle is illustrated in Fig. 4.

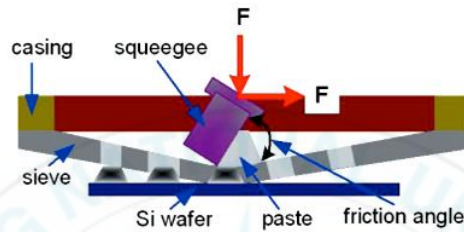


Fig. 4 The screen printing method [11]

The viscous property is a key of screen printing paste. The paste must be fluid enough to fill the mesh opening of screen without voids. However the as-printed paste must not spread over the surface. Critical parameters of screen printing process are the distance apart between screen and wafer, the pressure applied on the screen, and the velocity of the squeegee. However, the thin and non-homogeneous finger electrodes are produced due to the contact printing and mesh mark [13, 14]. Moreover the wafer thickness will have been getting thinner than 150 μm , contact printing likes screen printing trends to break wafer easily. For the next generation metallization, inkjet, aerosol and dispensing printing which are non-contact printing techniques have been considered.

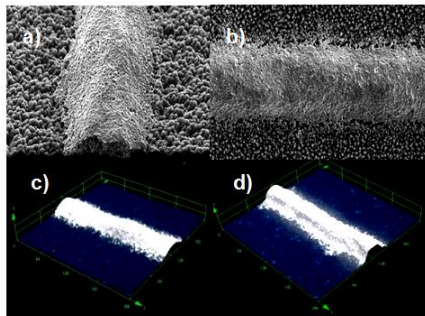


Fig. 5 a) Cross section b) top view of finger electrode by screen printing [12] c) 3D profile of single and d) double screen printing finger electrode [13]

2.1.4 Ink-jet printing

Ink-jet printing can be classified into 2 major processes: continuous ink-jet (CIJ) and drop-on demand (DOD) technology.

CIJ process starts by forming ink droplet from a continuously flowing jet of ink which driven through nozzle. The process starts with high pressure pumping that directs liquid ink from a reservoir forcing the liquid to leave flow a nozzle as a form of jet (Fig.6). The size of formed drops and the break up point are controlled by piezoelectric transducer.

The degree of the drop deflection is determined by the electric field strength which depends on the voltage applied and the distance between the field plates. This way is produced one line of the image to be printed. By moving the substrate, several lines are successively printed forming the desired image or text. In a more complex system, more jets can be couple to obtain a faster printing [15, 16].

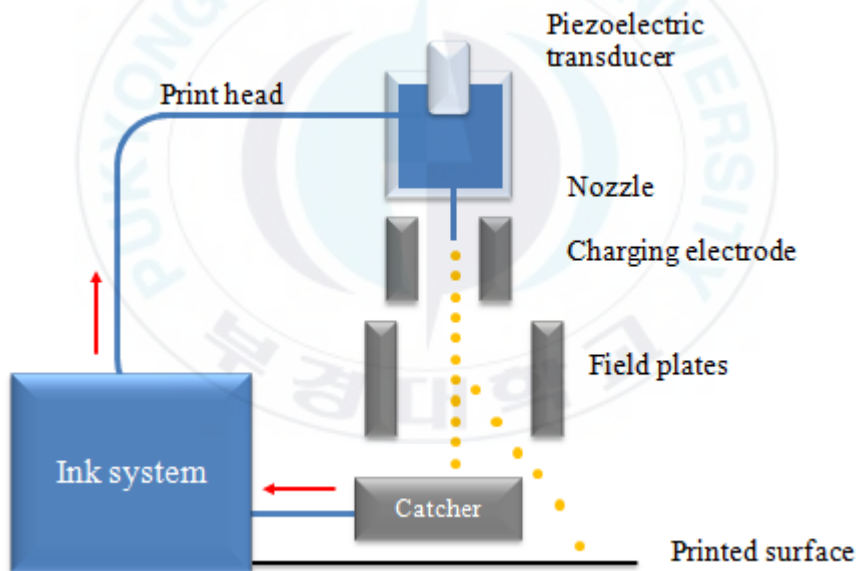


Fig. 6 Schematic diagram of continuous ink-jet (CIJ) printer

Currently, this printing technique is used to apply some information, as product name, date or batch codes. It cannot use in the print electronics due to the contamination of the ink which exposure to the environment as recycling process.

DOD system generated drop ink by piezoelectric material which is used to be an actuator only when an actuation pulse is provided. This material converts the applied externally electrical energy into mechanical deformation of an ink chamber (Fig. 7). An ink-jet method offers narrow and smooth finger electrode, avoidance the degradation of p-n junction at low temperature firing, mask free and uniform electrode on silicon solar cell [17, 18]. The complicated hardware for charging electrodes, break up the jet, deflection plates, capture and recirculation systems and high pressure pumps can be cut off by using DOD printers.

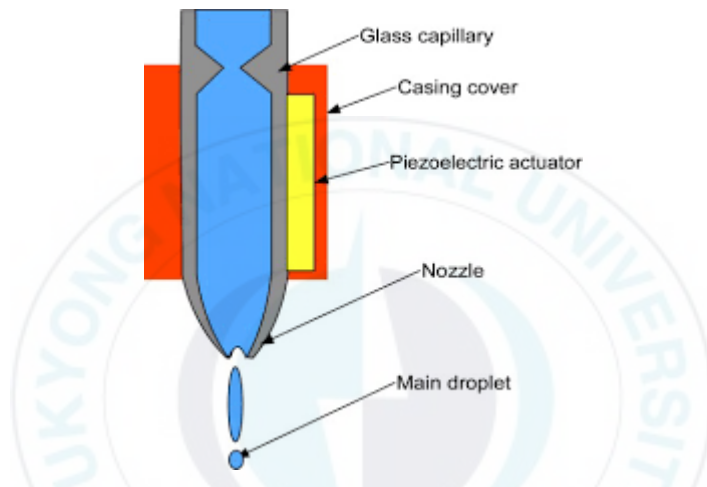


Fig. 7 Schematic model of piezoelectric ink-jet printing [19]

Teng and Vest (1998) were the first recorders for constructing finger electrodes on solar cell wafer by using direct ink-jet metallization with metallo-organic ink [20], and reported efficiency on multicrystalline silicon solar cell without ARC (SiN_x) layer was 8.08%.

Nevertheless, there are several critical issues of ink-jet metallization. The standard silver paste cannot be used due to the large silver particle size (5-10 μm), leading to the nozzle clogging problem. As a general guideline, the nozzle diameter should be at least 6 times larger than particle size. So, resulting finger electrode with would be wider [21].

2.1.5 Aerosol jet printing

Aerosol jet printing is a direct printing technique which an ink should be nebulizable. There are 2 options to generate aerosol: ultrasonic and pneumatic atomizer [22].

Fig. 8 shows the working principle of ultrasonic atomize. For this approach, the high frequency pressure waves from the piezoelectric transducer are generated and directly transferred through water to the bottle with the ink. The atomized droplets are generated by the pinched off of capillary wave. Then the atomization of small droplets are transported to the deposition head.

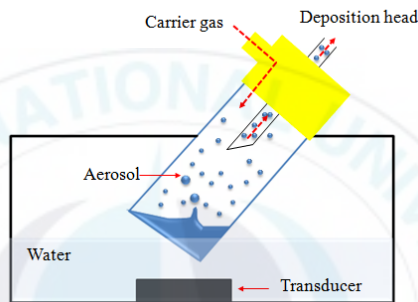


Fig. 8 Schematic model of ultrasonic atomizer principle

For pneumatic atomizer, a high velocity gas stream is produced by the expanding of compressed gas through the nozzle. Subsequently, the liquid stream was broken into droplets by this gas stream and suspended them in the flow. The large droplets are removed by strike against the side walls of reservoir. The remaining of smaller droplets are transported to the deposition head [23].

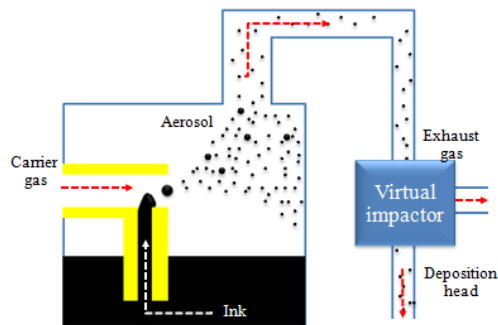


Fig. 9 Schematic model of the pneumatic atomizer principle

In contrast with an inkjet technology, nebulize are generated and moved to the deposition head via a heatable tube which can adjust the viscosity of ink. In this printing head, the avoidance between metal aerosols being contact with the nozzle tip can be occurred by wrapping up of ring shape gas. It is main approach for the aerosol printed line width to be narrower than nozzle diameter. In order to control the fluid flow in the print head, the adaptation of sheath gas to aerosol-flow ratio is required. By adjusting this ratio, a narrow jet can be generated [24]. The working principle of by aerosol printing is shown in Fig. 10.

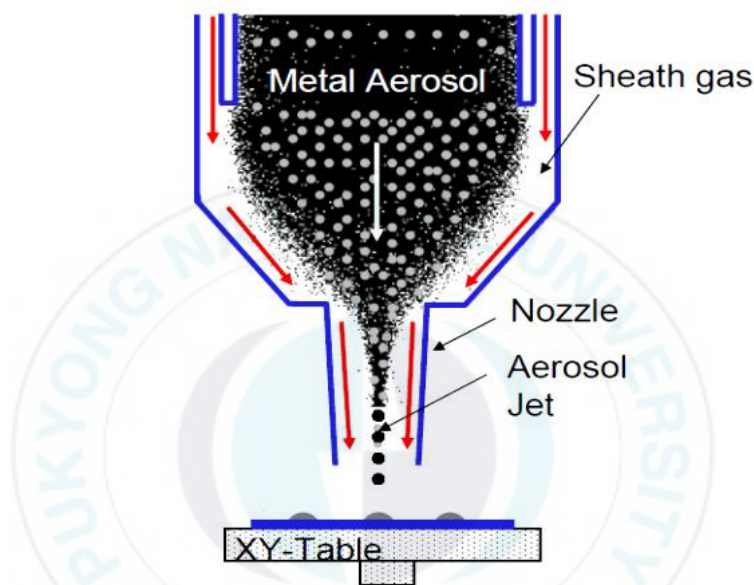


Fig. 10 Metallization by aerosol printing [25]

The main advantages for working principle of aerosol printing is gas stream which surrounds metal paste and focuses through the nozzle to substrate. The clogging of nozzle tip can be prevented by this gas. Moreover the ultrafine finger electrode can be constructed even much narrower than the size of nozzle diameter. It has been recorded by using a nozzle with the 200 μm nozzle in diameter with printed lines of 50 μm width can be achieved [26]. According to A. Mette et al. experiment [23], the energy conversion efficiencies up to 17.8% on $12.5 \times 12.5 \text{ cm}^2$ by size of monocrystalline silicon solar cell with an aluminium back surface filed has been recorded.

Nevertheless, single-pass printing of inkjet and aerosol printing techniques cannot construct high aspect ratio electrode. Thin finger electrode throughput from both techniques effects on the power losses of solar cell [27].

2.1.6 Dispensing printing

As opposed to screen printing approaches, homogeneous finger electrode is achieved by dispensing printing technique. The dispensing printing offers single step metallization with high aspect ratio and significantly reducing finger electrode width results in higher cell efficiency [28]. It also requires less silver consumption than screen printing technique [29].

The rheology of silver paste plays the main influence of dispensing printing technique. Due to the non-contact printing, the pastes are free flow which results in recovery the process of silver paste [30]. The dispensing technique also offers the possibility to adjust the rheological of silver paste. According to the P. Maximilian et al. experiment [31], the dispensed three silver pastes with different yield strength out of 40 μm nozzle in diameter by increase the yield stress and young modulus from paste A to C are shown in Fig. 11, the optical finger line width is decrease from 40.4 μm to 30.7 μm . He also reported that even though finger line width in paste C is the narrowest, the contact resistance in paste C is higher due to the necking. Maximilian concluded that the paste B is the best.

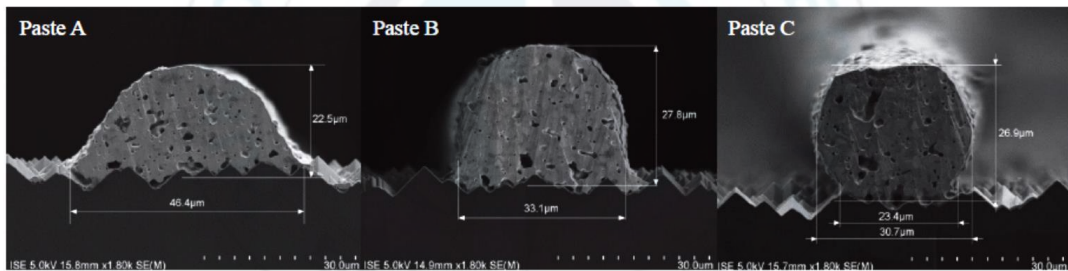


Fig. 11 The adaptation of paste rheology with difference yield stress and young modulus from paste A to C [31]

Further rheology development of Maximilian silver paste, leads to achieve the finger electrode down to 27 μm in width in 2011 (Fig. 12a)). The cell efficiency is as high as 20.6% since high aspect ratio and mesh mark free likes screen printing. The throughput was increased by using multi nozzle print heads as shown in Fig. 12b) [32].

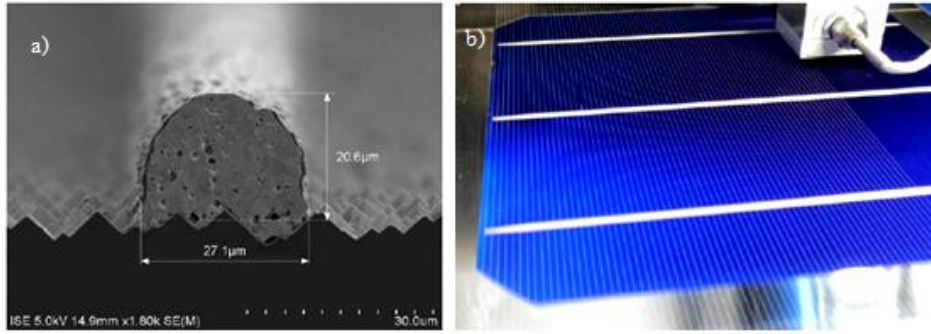


Fig. 12 a) SEM image of the rheology development silver paste which dispensed through 40 μm nozzle diameter b) Parallel 10-nozzle dispensing unit during cell fabrication [32].

Beside of rheology, the finger line widths are affected by nozzle size, dispensing speed, pressure and gap between nozzle and wafer. K. Do-Hyung et al. [14] reported his experiment that the finger line widths were decreased by using small nozzle and reducing the dispensing pressure, and also by increase the dispensing speed and gap between nozzle and wafer. He also suggested the using of small nozzle size and lower pressure to get higher aspect ratio.

However the disruption of dispensed silver paste during printing has been a hurdle in the art. To mitigate this problem, carbon nanofiber (CNF) has been considered to increase the elongational property.

2.2 Carbon nanofiber (CNF)

Table 1 Comparison price and length of nanofiber [33]

Nanofiber	Cost (\$/g)	Length (μm)
Graphite nanofiber	3	10-30
Multi Walled Carbon Nanotube	3	~ 10
Single Walled Carbon Nanotube	300	~ 10
Silver nanowires	495	~ 30

Among the nanoscale of carbon type, there are 2 candidates which is cost effectiveness. However CNF shows more excellent benefits than multiwall carbon nanotube (MWCNT) and single wall carbon nanotube (SWCNT) in the term of process. Moreover it is easier to disperse due to the feature exposed of graphene planes on the surface which can be readily modified through the thermal treatments or chemical functionalization without scale-up process. On the other hand, the first creating defect along the side walls of other fiber is required for attaching functional groups, which is time consuming and costly process [34].

Carbon nanofiber (CNF) is a high aspect ratio filament which excellent in mechanical properties, electrical and thermal conductivity in polymer composite [35]. Due to its low cost and availability, it has been studied to be reinforcement in composite materials. Despite of the fascinating characteristics, the used of CNF in composite has been limited by several challenges. It is difficult to uniformly disperse CNF and Van der Waal interaction of CNF which induces the CNF agglomeration [36].

2.2.1 Synthesis and structure of CNF

The mainly preparation of CNF has 2 approaches. One is the cup-stacked CNF or catalytic thermal chemical vapor deposition (Fig. 13). Several types of alloy or metal which can dissolve CNF has been used to form metal carbide. Additional the gas containing carbon such as carbon monoxide, methane or ethane are used in the temperature range from 130-930°C to provide the carbon sources. The growth mechanism has been justified by the deposition of hydrocarbon dissolved in the metal particle and precipitate on the metal substrate.

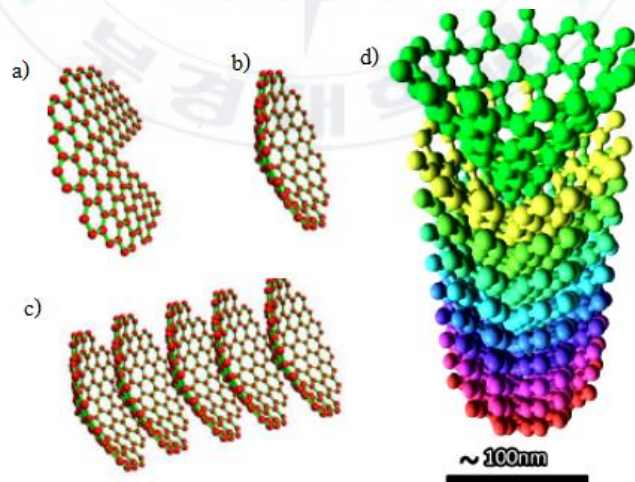


Fig. 13 The stacked-cup of CNF structure formation [37]

In order to fabricate CNF by electrospinning method, polymer nanofibers are required to be precursors. The properties of final CNF depend on size of polymer and process parameter such as atmosphere and temperature [37].

Generally the electrical resistivity of CNF depends on the type, diameter and temperature. Endo et al. [38] measured the electrical resistivity of short-grown carbon fibers (VGCF-S) via four-point-probe method. The result showed the electrical resistivity of VGCF-S is in range 10^{-3} to 10^{-6} Ω .cm. At 20°C the electrical resistivity of CNF (2.5×10^{-4} to 5.0×10^{-4} Ω .cm) is higher than the electrical resistivity of silver (1.59×10^{-6} Ω .cm) about 250 times. The increase of temperature is effect on the decrease of electrical resistivity of CNF [39]. However the CNF contains amorphous and impurity that could degrade its electrical properties. In order to increase the crystallinity and remove the impurities, the heat treatment is required. Hereman et al. [36] reported the electrical resistivity of the heat treat CNF at 2900°C was as low as 6.8×10^{-5} Ω .cm.

In the solar cell applications, C. Xi et al. reported that the cell efficiency was improved by integration of 1D-GCNF at the rear side of silicon solar cell with specific thickness. They explained that GCNF provided a significant improvement long wavelength back scattering by the bent of carbon layer on surface [40]. Due to the exceptional properties, CNF has great potential to improve efficiency on the state-of-the-art of solar cell

3. Experimental

In order to understand the influence of CNF in the silver paste, the in-house developed and commercially available silver paste were prepared. Their physical and electrical characteristics were investigated in this study.

3.1 Characterization of CNF

The different source of carbon nanofiber (CNF) may have different characteristics. In this study, the CNF (GNF-L) from Carbon Nano-material Technology Co., LTD., Republic of Korea which is the additional composition in silver paste was characterized by various techniques in order to analyze microstructure and thermal property.

3.1.1 Microstructure characterization of CNF by Transmission Electron Microscope (TEM)

TEM is a microscope technique which uses high energy electron beam to transmit through the thin specimen. When the electron passes through an ultra-thin specimen, electrons are scattered. A high resolution image is focused by a sophisticated system of electromagnetic lenses.

In this experiment, CNF (GNF-L, Carbon Nano-material Technology Co., LTD., Republic of Korea) was analyzed by using TEM (Joel JEM-2010 instrument, Japan).

3.1.2 Thermo gravimetric analysis (TGA) of CNF

TGA is a technique to analyze the stability of materials. The chemical or physical of materials is changed when the temperature is increased with constant heat rate. TGA is used to determine the characteristic by measurement the mass loss or gain due to decomposition, loss of volatiles, or oxidation.

The sample is loaded in the small pan which connected to a precision balance. The temperature and atmosphere can be controlled by programmable furnace. Due to the decomposition or oxidation of various components in sample, the weight percentage of mass change can be measure with increase temperature.

In this experiment, CNF (GNF-L, Carbon Nano-material Technology Co., LTD., Republic of Korea) and the mixture of CNF with other ingredients were analyzed by using TGA (Perkin–Elmer, Pyris 1, U.S.A) in dry air with air flow rate of 20 ml/min. The temperature was increased at 10°C/min.

3.2 Preparation of silver paste

There are 3 mainly composition of silver paste: silver powder as a conductive particles, glass frit and carrier vehicle. Normally, the silver electrode was placed at the front side of solar cell wafer but the adhesion force between silver powder and crystalline silicon solar cell wafer is very poor. The carrier vehicle was induced to increase the adhesion between silver powder and crystalline silicon wafer due to the wettability of solvent. Then the organic compound was burnt out after firing or drying.

3.2.1 The preparation of in-house developed silver paste

Three kinds of the in-house developed silver pastes were prepared with different weight fractions of CNF (0, 0.2 and 0.5 wt%) to silver.

3.2.1.1 The carrier vehicle preparation

In this study carrier vehicle consists of Ethylcellulose (EC300, Order No. 200646, Sigma-Aldrich Corp., USA), polyamide thixotrope (TMAX, Elementis Specialties, Inc., USA), 2 kinds of dispersion (FC4430: ovecTM Fluorosurfactant, Energy and Advanced Materials Division, 3M, USA and PD2246, Croda International Plc., UK) and solvent (α -terpineol, CAS No. 98-55-5, Kanto Chemical co., Inc., Japan) was prepared in different fraction. The diagram to prepare carrier vehicle is shown in Fig. 14.

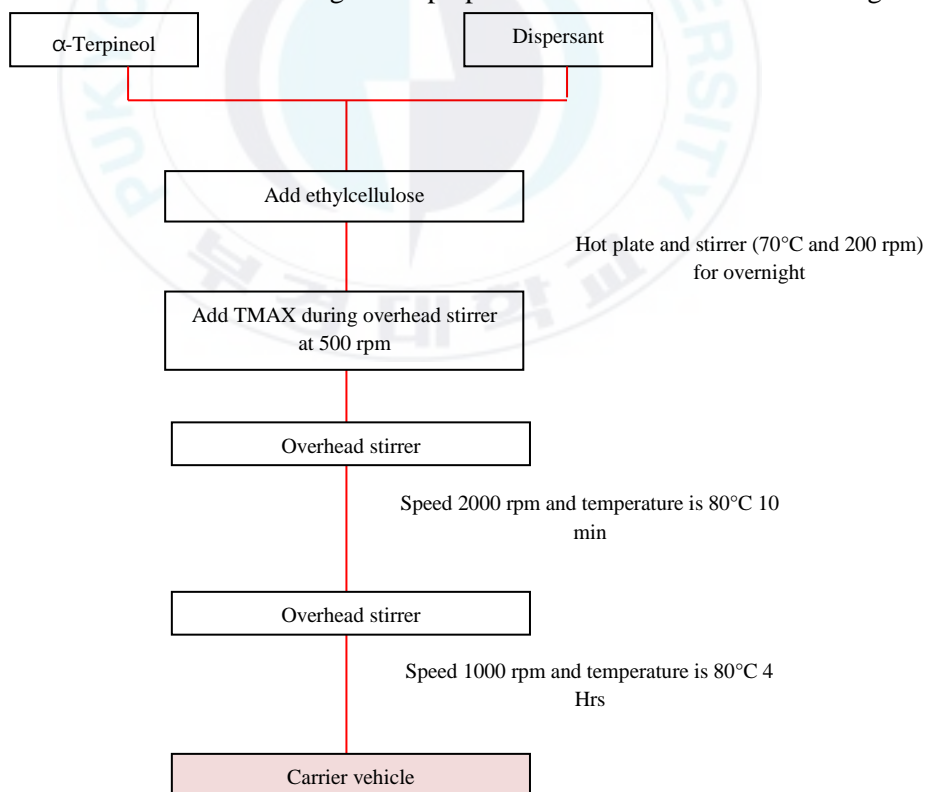


Fig. 14 Carrier vehicle process chart

According to the Fig. 14, after α -terpineol and 2 kinds of dispersants (FC4430 and PD2246) were put into the same glass bottle and placed on the hotplate and stirrer (70°C and 200 rpm), the ethylcellulose was added during hotplate and stirrer process. Then the mixture was left on the hotplate and stirrer overnight. While the mixture was overhead stirred at 500 rpm, the TMAX was added. The mixture was overhead stirred at speed 2000 rpm and 80°C for 10 min. Finally, the mixture was overhead stirred at speed 1000 rpm and 80°C for 4 Hrs. The weight fraction of three carrier vehicles is shown in table 2.

Table 2 Three different composition of carrier vehicle

Carrier vehicle no.	Solid content (wt %)	Composition (wt%)				
		EC300	TMAX	PD2246	FC4430	Terpineol
1	90	0.3	1	1	0.5	8.31
2	90	0.3	1	1	0.5	8.11
3	90	0.3	1	1	0.5	7.81

3.2.1.2 Glass frit preparation

The comparison between different size of glass frit shown that fill factor and cell efficiency were improved with the solar cells based on nanosize glass frit powder. Due to nanosize glass frit is easier to wet and melt on the silicon substrate. So the SiN_x was homogeneously etched, less pore and silver crystallites at the silver-silicon interface are advantageous for good ohmic contact of front side metallization [41, 42, 43].

In order to make smaller particle size of glass frit, the glass frit (GF-V2172, Ceradyne Inc., USA) was pulverized by using Fritsch pulverization (Planetary Micro Mill PULVERISETTE 7 premium line), as shown in Fig. 15a). There are 2 bowls; container bowl and balance bowl.

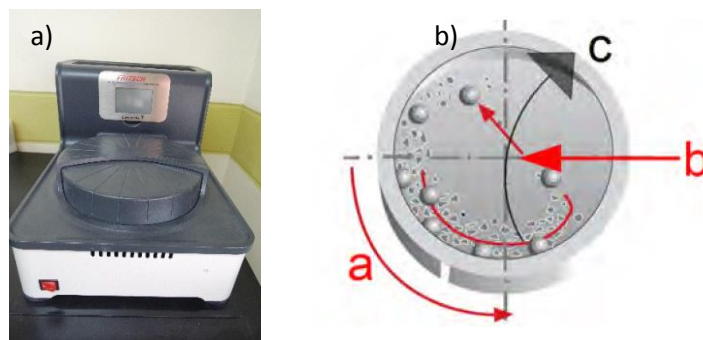


Fig. 15 a) Planetary Micro Mill PULVERISETTE 7 premium line b) Theory of grinding [44]

By centrifugal forces rotation of grinding bowls and the support disc which rotates in the opposite direction with grinding bowl. Therefore ball hit the opposite wall of bowl, resulting in the source material is crushed with an impact effect.

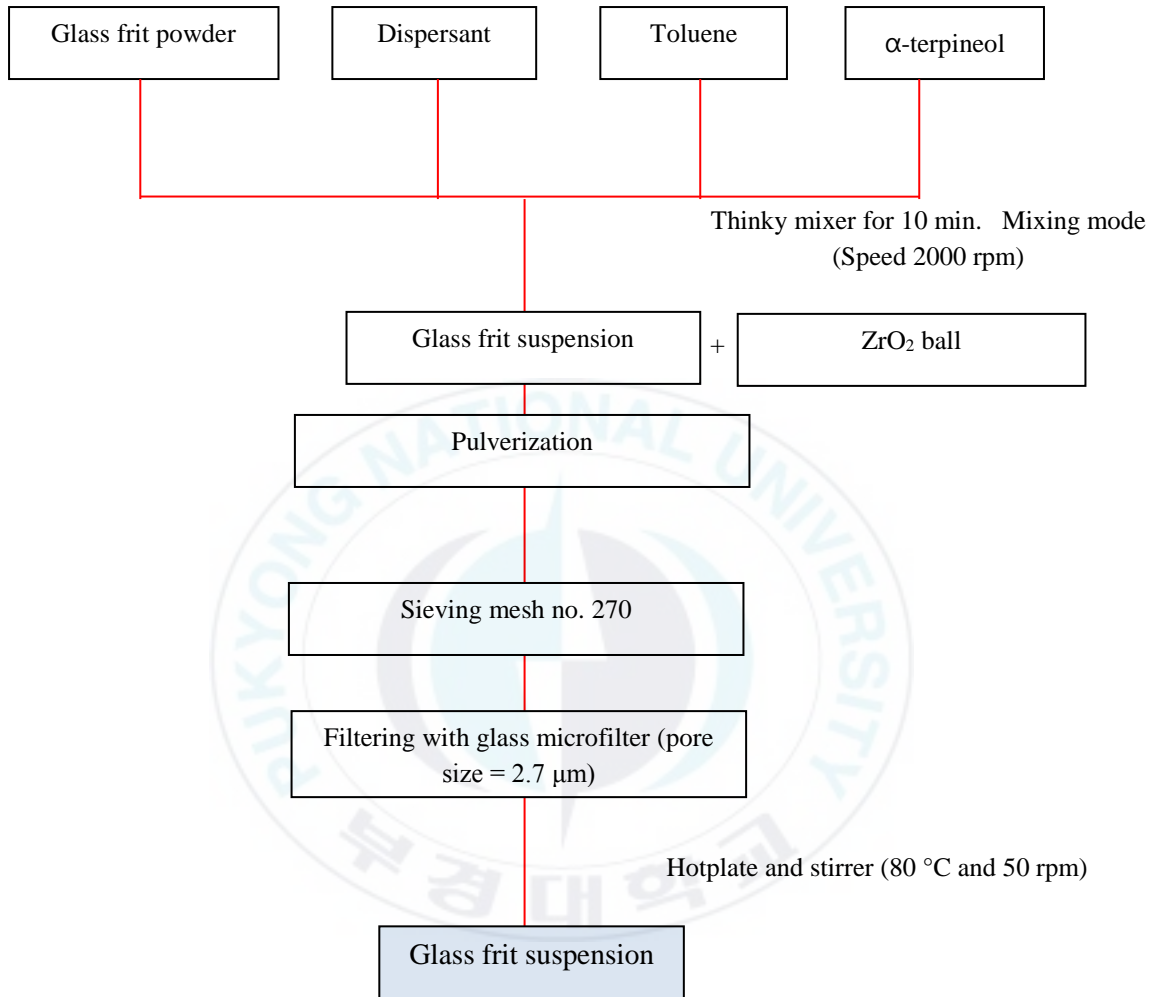


Fig. 16 Process chart to make concentrate glass frit

According to the Fig. 16, the 60% concentration of glass frit suspension composition consists of GFV2172, Toluene, Terpeneol and dispersion (PD2246), was mixed together by thinky mixer with mixing mode at speed 2000 rpm for 10 min. The mixed suspension was poured into the containing bowl and pulverized with ZrO₂ ball which diameter 0.5 mm (1:5 of glass frit to ZrO₂ ball) for 10 cycles, each cycle pulverized 10 min for setting time and pulse time. Then the pulverized suspension was sieved with sieve mesh no. 270 to separate ZrO₂ ball. The glass microfiber filter which pore size 2.7 μm was used to filter the glass frit suspension. Finally, the suspension which particle size less than 2.7 μm was put on the hotplate and stirrer to make concentration of glass frit suspension. The composition of glass frit suspension in this experiment is shown in table 3.

Table 3 The composition of glass frit suspension

Composition of glass frit suspension (wt%)			
GFV2172	PD2246	Toluene	Terpineol
60	1	30	10

3.2.1.3 In-house silver paste preparation

Carrier vehicle, ZnO, glass frit suspension and CNF were mixed by thinky mixer for 10 min with mixing mode at speed 2000 rpm. Then the mixture was 3 roll milled for 6 min (feed and apron roll gap is 10 μm). Next, the 3 roll milled silver paste was mixed by thinky mixture with 2 different mode, mixing and de-foaming mode. After aging for 1 day on roll mixer, the silver particle was added into the mixture. The mixed silver particle and the carrier vehicle was 3 roll milled for 6 min to disperse silver particle and form homogeneous silver paste. Finally, the homogeneous paste was thinky mixed and aged for 3 days. The process flow of silver paste preparation is shown in Fig. 17.

In this experiment, 0, 0.2 and 0.5 wt% CNF pastes were prepared. The concentration of glass frit suspension is 81.56% for 0 and 0.2 wt% CNF paste and 80.94% for 0.5 wt% CNF paste. The carrier vehicle number 1, 2 and 3 were used for 0, 0.2 and 0.5 wt% CNF paste, respectively. The composition of silver paste is shown in Table 4.

Table 4 Silver paste composition

Carrier vehicle no.	wt%		Glass frit suspension (%)
	CNF concentration	ZnO	
1	0	5	81.56
2	0.2	5	81.56
3	0.5	5	80.94

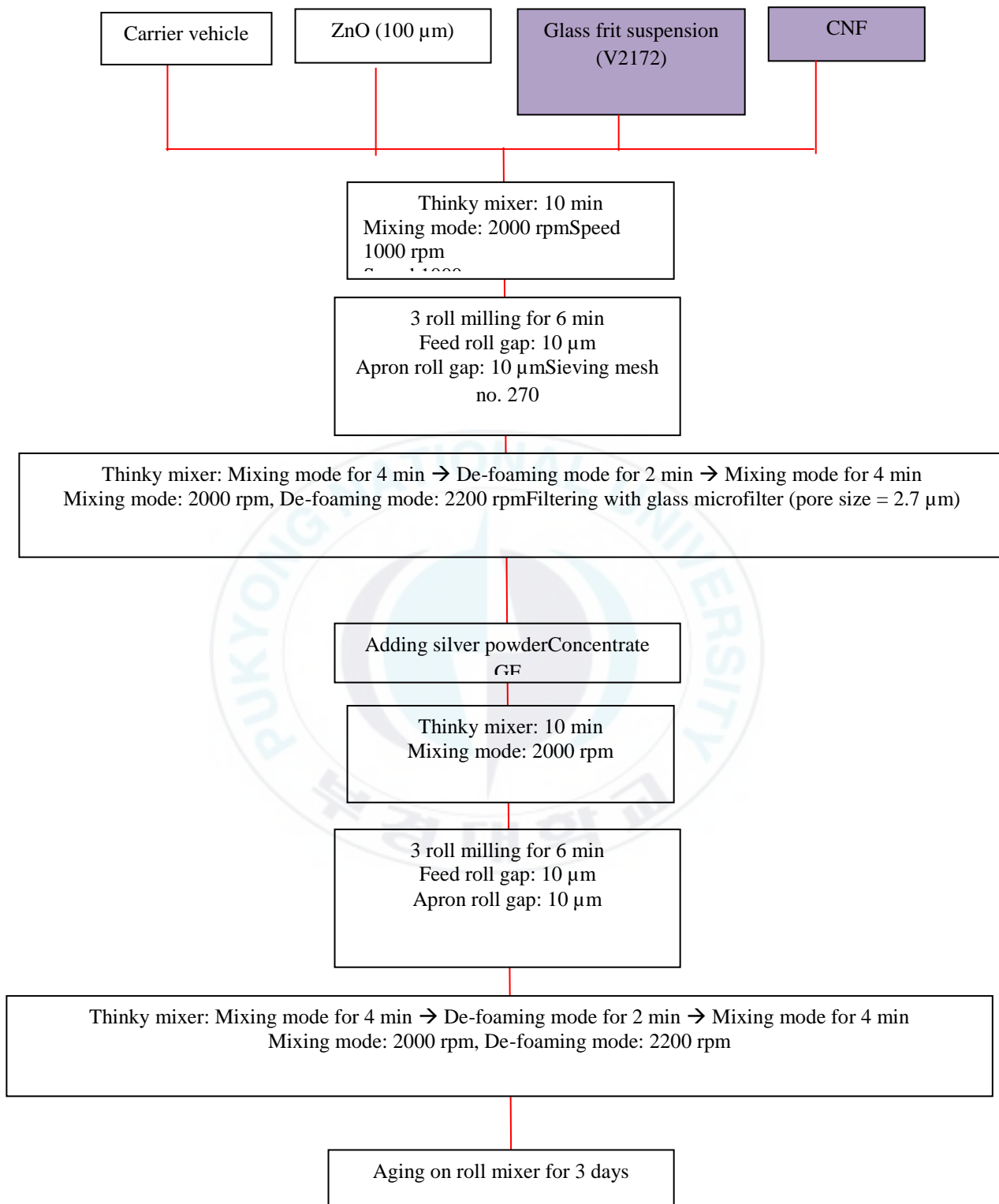


Fig. 17 The silver paste with glass frit pulverization

3.2.2 Preparation of commercially available silver paste containing CNF

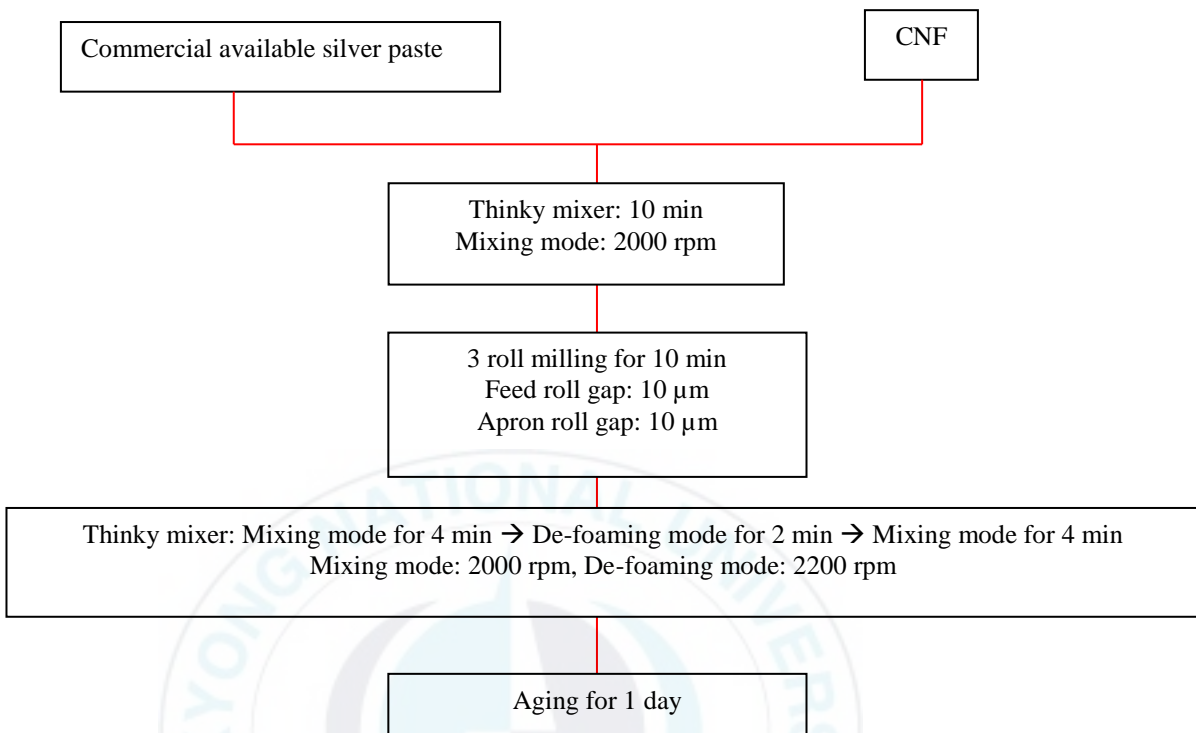


Fig. 18 The process flow of commercially available silver paste containing CNF

The CNF was added into the commercially available silver paste at different weight fraction, 0, 0.2, 0.4 and 0.6 wt%. After thinky mixing (Fig. 19a), the commercially available silver pastes containing CNF were 3 roll milled (Fig. 19b) for 6 min (feed and apron roll gap is 10 μm). The homogeneous silver pastes was mixed by thinky mixer and aging for 1 day. The diagram of commercially available silver paste containing CNF is shown in Fig. 18.

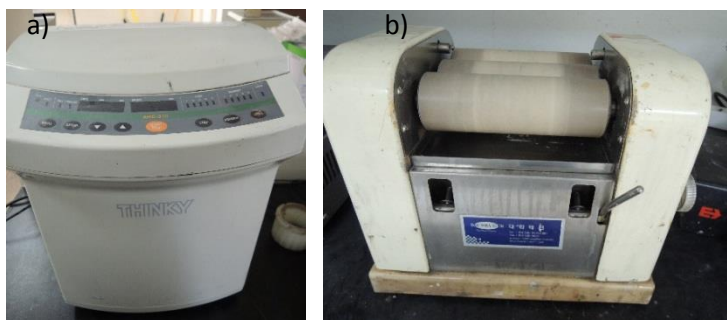


Fig. 19 a) Thinky mixer (Thinky, ARE-310, Japan) and b) 3 roll mill (EXAKT Technologies, Inc., EXAKT-50, USA)

3.3 Fabrication of crystalline silicon solar cells

The process flow for fabrication of crystalline silicon solar cell is shown in Fig. 20. Monocrystalline silicon solar cell wafers with an emitter sheet resistance of $80\Omega/\text{sq}$ were used for measuring the cell efficiency. After an aluminium paste was screen-printed (DaeyeongHitech, Tiger-5335MV-1S) on the back side of monocrystalline silicon solar cell wafer and dried on a hot plate (DHSL Korea Co., Ltd., DHSL.HP2020300, Republic of Korea) at $150\text{ }^\circ\text{C}$ for 7 min, three busbars were screen-printed with a commercially available silver paste on the front side of the monocrystalline silicon solar cell wafer and dried on a hotplate at $150\text{ }^\circ\text{C}$ for 3 min. To evaluate the cell efficiency, the silver paste containing CNF at different fraction was dispensed with 75 and 50 μm nozzle diameter ceramic nozzle. The printing speed was 100 mm/s with a powerful screw pumping motor (AMD3-CEC-YD 100 W, Eser Corp., Japan). The electrode spacing was set to be 1.5 and 2 mm, dried at $150\text{ }^\circ\text{C}$ for 5 min on a hot plate [26].

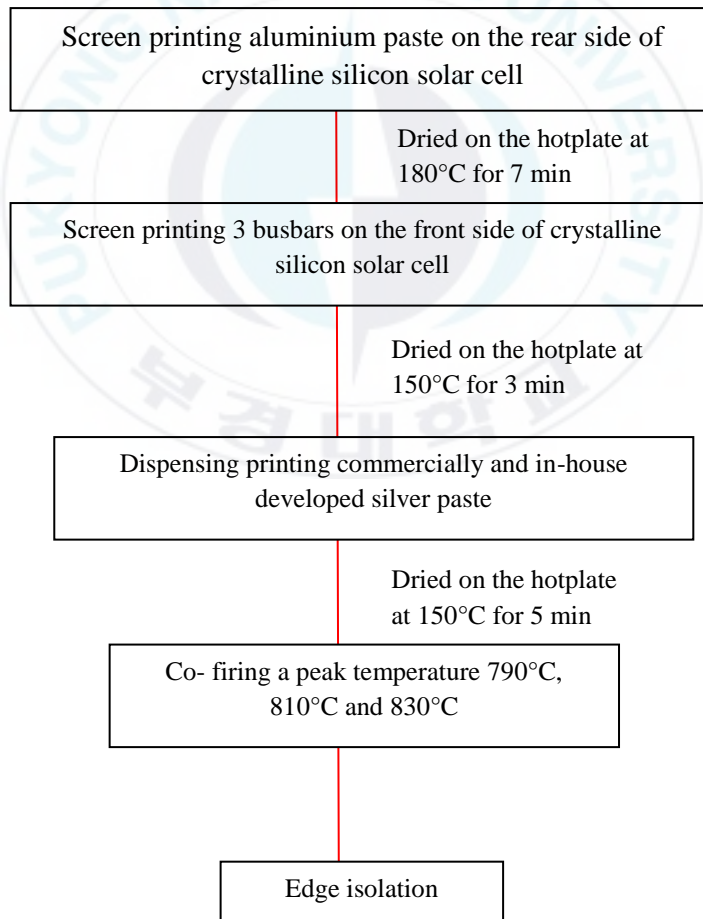


Fig. 20 Fabrication of crystalline silicon solar cell process chart

Due to the different formation temperature at front and rear side of solar cell during co-firing, the peak temperature and ramp up rate should to be considered. During firing process antireflection coating (SiN_x) is etched by glass frit and formed the contact between silver and silicon substrate at front side. For the backside, Sopori et al. reported that the silicon diffuses, reacts with aluminium at the rear side and the back surface field is formed at temperature $755 - 800^\circ\text{C}$ [45]. Taeyoung Kwon et al. found that the increase of ramp up rate and properly by setting the belt speed furnace improved higher open circuit voltage. He also reported that the higher ramp up rate also provided the uniformity of back surface field layer [46].

Therefore, the as-printed electrodes were co-fired at a peak temperature 790°C , 810°C and 830°C by using a rapid thermal processor (RTP: AccuThermo AW 610, Allwin21 Corp., USA) (Fig. 21) with ramp-up rate of $100^\circ\text{C}/\text{sec}$ in the ambient air.



Fig. 21 Rapid thermal processing system

The front and back contacts would be interconnect with the n-type region at the edges of solar cell, leading to lower shunt resistance. To remove this region, the junction isolation is required. In this experiment, laser isolation was performed at the edge of silicon solar cell wafer by using a 532-nm laser (NANIO 532-10-V, InnoLas Laser GmbH, Germany) and a 2-axis laser scanner (SS-II-10, Raylase AG, Germany). Finally, solar cell wafers were etched with KOH solution at the edge of wafer and dry at 150 °C for 5 min on a hotplate.

The finger line width at each weight fraction of CNF in different silver pastes was measured by using zoom stereo microscope (JSZ-7XT, Samwon Scientific Ind. Co., Ltd., Republic of Korea), is shown in Fig. 22.



Fig. 22 Zoom stereo microscope

3.4 Electrical characterization

The electrical properties of commercially available silver paste with and without CNF have been investigated in order to understand the role of the additional CNF in silver paste to determine the contact resistivity between finger electrode and silicon solar cell wafer, and resistivity of silver paste containing CNF.

3.4.1 Contact resistivity characterization

The electrical properties were evaluated using a probe station (MST 4000 A, MS Tech Co., Ltd., Republic of Korea) and a source meter (Model 2401, Keithley Instruments Inc., USA). The contact resistivity was determined by Transfer Line Method (TLM) measurement.

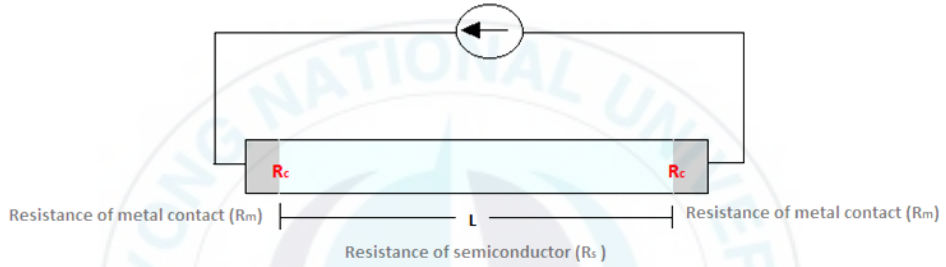


Fig. 23 Total resistance components

According to the Fig. 23, the gray rectangles are shown the metalized contacts on the sample. The measurement of total resistance consists of several components, the resistance of contact metal (R_m), the resistance between metal and semiconductor interface (R_c) and the resistance of semiconductor (R_{semi}).

$$R_t = 2R_m + 2R_c + R_{semi} \quad [1]$$

Generally, the resistance of metal in the contact is very low that $R_c \gg R_m$, and so R_m can be ignored;

$$R_t = 2R_c + R_{semi} \quad [2]$$

The resistance of probe itself, the resistance between probe and metal contact and the resistance of metal contact itself are much smaller than the resistance between metal and semiconductor interface, the total resistance becomes:

$$R_{semi} = \frac{R_s}{W} L \quad [3]$$

$$R_t = \frac{R_s}{W} L + 2R_c \quad [4]$$

When R_s is sheet resistance of semiconductor, L is grid spacing between metal contact and W is finger width.

The transfer length method (TLM) illustrated in Figures 24a) and 24b). If the metal contact (blue area in Fig. 24a)) has same doping with contact area of devices and array contact (grey in Fig. 23b)) with different spacing is formed over the doped region, the resistance measurement between 2 metal contacts can be used to construct TLM graph, as shown in Fig. 23b).

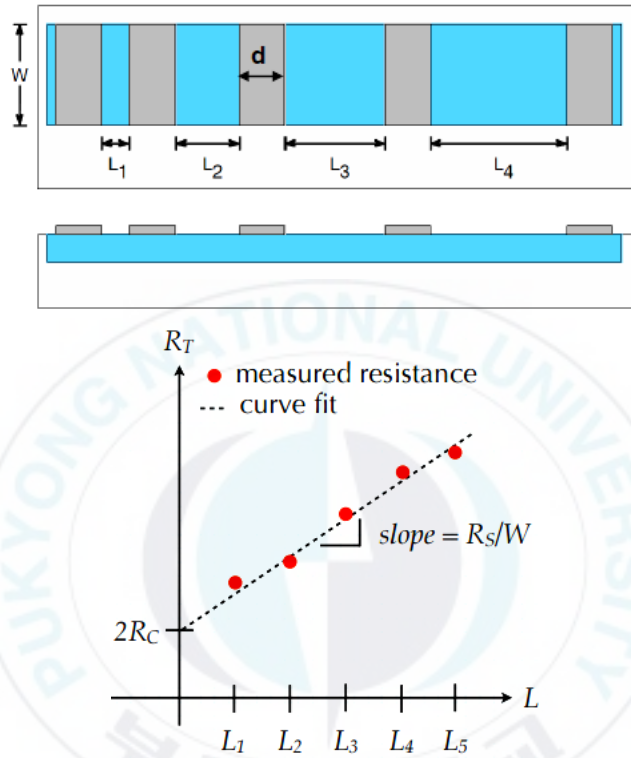


Fig. 24 a) TLM measurement and b) evaluation of the contact and sheet resistances for TLM measurement [47]

By extrapolating back to $L = 0$, the residual resistance is twice the contact resistance. Moreover, the sheet resistance (R_s) of the semiconductor can be calculated from the slope of the graph [47, 48].

In this study, the contact resistivity of constructed finger electrode with 0, 0.2, 0.4 and 0.6 wt% CNF in commercially available silver pastes on crystalline silicon solar cell sample $15 \times 25 \text{ mm}^2$ by size was investigated.

3.4.2 Resistivity

The resistivity of semiconductor is simple measured by four point probe. A current is supplied through the two outer probes; the voltage across the two inner probes are measured by voltmeter (Fig. 25).

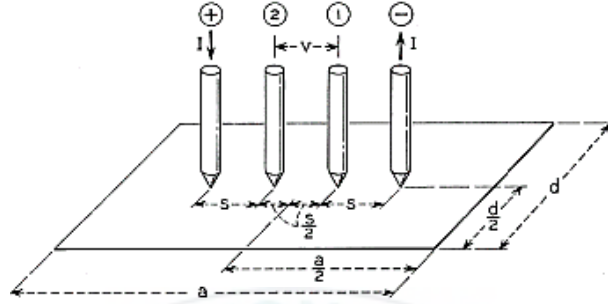


Fig. 25 Arrangement of a 4-point probe on a rectangular sample [49]

The resistivity (ρ) of silver paste as given in [5]

$$R_{sheet} = \frac{\rho}{t} \quad [5]$$

The ρ describes the relation between sheet resistance (R_{sheet}) and layer thickness (t). In order to get the ρ , R_{sheet} was determined by four point probe as given in [6]

$$R_{sheet} = \frac{\pi}{\ln 2} C_1 C_2 \frac{V}{I} \quad [6]$$

When C_1 is size correction factor which depends on the probe tip spacing (s) and the wafer diameter (d). C_2 is thickness correction factor. C_1 and C_2 correction factor is show in Table C-1 and C-2 in appendix C. V is voltage across inner probes (V) and I is current across outer probes (A).

In this study, the dilution of commercially available silver paste with different weight fraction of CNF to BCA at 9:1 ratio was spin coated on $2 \times 2 \text{ cm}^2$ by size of crystalline silicon solar cell at 3000 rpm for 20s. Then the sample was dried on the hotplate at 150°C for 5 min. The dried sample was firing at target peak temperature 810°C with ramp-up rate 100°C/s . The layer thickness was calculated from the different thickness between firing and before coating sample. Finally, the resistivity was determined by four point probe (4 Point Probe One Body type, MS Tech Co., Ltd., and Republic of Korea) measurement and sourcemeter (401 Low Voltage SourceMeter Instrument, KEITHLEY, U.S.), as shown in Fig. 26.



Fig. 26 Four point probe and sourcemeter using for measuring the resistivity

3.5 Morphological characterization

3.5.1 Scanning Electron microscope (SEM)

The basic principle of SEM is that a high voltage (e.g.: 20 kV) accelerates electron beam which is generated from suitable source, typically emission gun or tungsten filament. The thin beam of electrons for scanning surface of the specimen is produced by accelerated electron beam which passes through a system of apertures and electromagnetic lenses. The action between electron beam and specimen causes electron emitting which is collected by a suitably-positioned detector.

To investigate the effect of CNF residue on electrical properties of finger electrode, the finger electrode with and without CNF was observed by SEM (S-2400, HITACHI, Japan). In this study, the SEM image of dispensed commercially available cell was compared to commercially available cell containing CNF.

3.5.2 Field Emission-Scanning Electron Microscopy (FE-SEM)

As the same principal with SEM, FE-SEM provides narrower probing beams, resulting in minimized sample charging and damage and improved clearer resolution.

The mixture of glass frit (GFV2172) to CNF at 1:1 volume ratio was prepared to understand the behavior of CNF in silver electrode by gentle grinding with mortar. Its characteristic was compared by using FESEM (JEOL, JSM-6700F, USA).

3.6 Rheological characterization

The torque is required force to rotate a cone or plate with fluid. Therefore the known speed is a function of the viscosity of that fluid. A graph is plotted between shear stress (torque) and shear strain rate.

Shear rheological measurement were made using a HAAKE MARS 60 Rheometer from Thermo Scientific™, USA (Fig. 27) with 77 mm length of titanium plate and cone (P35 Ti L). The viscosities of different weight CNF concentration silver pastes were measured at shear rates from 10^{-5} to 10^{10} s^{-1} . In this experiment, all the measurements were done at 25°C.

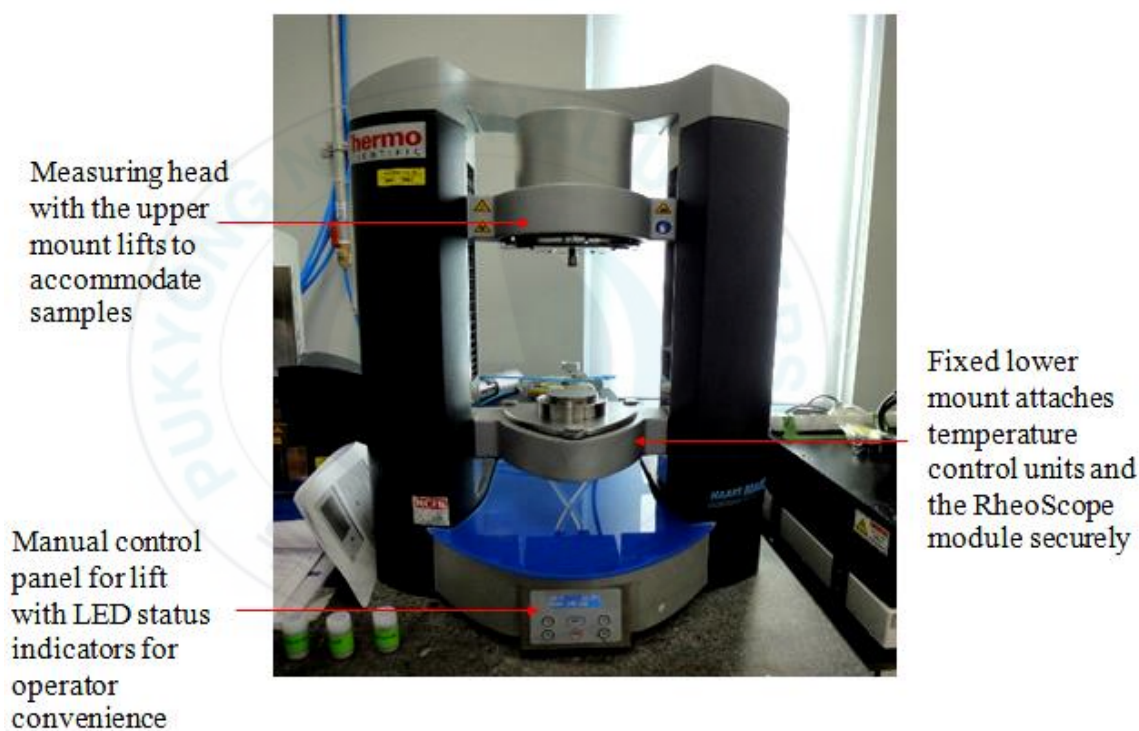


Fig. 27 HAAKE MARS 60 Rheometer using for rheological characterization

3.7 Solar cell Efficiency

The prepared solar cells with 0.2 wt% CNF and without CNF at 2 mm grid spacing, each 5 wafers were firing at difference peak temperature of 790, 810 and 830°C and compared their characteristics. The cell efficiency (η) was confirmed by Korea Institute of Energy Research (KIER).

4. Result and discussion

4.1 Microstructure of CNF

As-received CNF, purified by supplier, was found by using Transmission Electron Microscope (TEM) to contain highly entangle agglomerate but no visible impurity, as shown in Fig. 28. Almost individual CNF was not straight, forming clumps with a characteristic size of 300nm in length. These clumps were often clusters to form larger aggregates with diameter up to millimeter. The diameter of CNF was rather uniform about 30 nm in average with higher aspect-ratio than 100 [33]. Due to the CNF was so entangled, the network structure was formed and it was difficult to find both end of single nanofiber. Moreover the dispersant of CNF is known to be difficult. However the CNF can be incorporated into silver paste directly without significant manufacturing development. Another benefit provides the addition of CNF improved the elongational property.

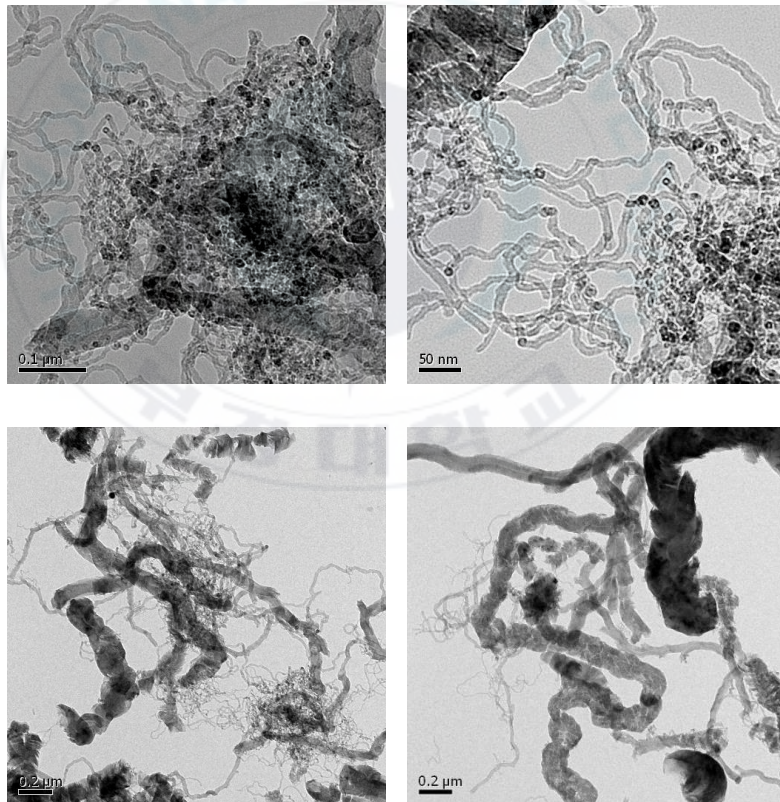


Fig. 28 TEM image of as-received CNF

4.2 The effect of CNF on rheology of silver paste

Fig. 29) demonstrates the flow curve (shear viscosity versus the applied shear strain rate). Since the shear flow, the entangled network of CNF that individually alignment in the flow direction thus the network breaking up higher shear strain rate, resulting in shear thinning over the entire range of shear strain rate [50]. Due to the geometrical effects, the incorporation of CNF in silver pastes was highly viscosity. As the CNF increases, the silver pastes behave as solid and therefore the viscosity of silver paste proportionally increases [51, 52]. A brief viscosity characterization is presented, with details covered in Appendix A.

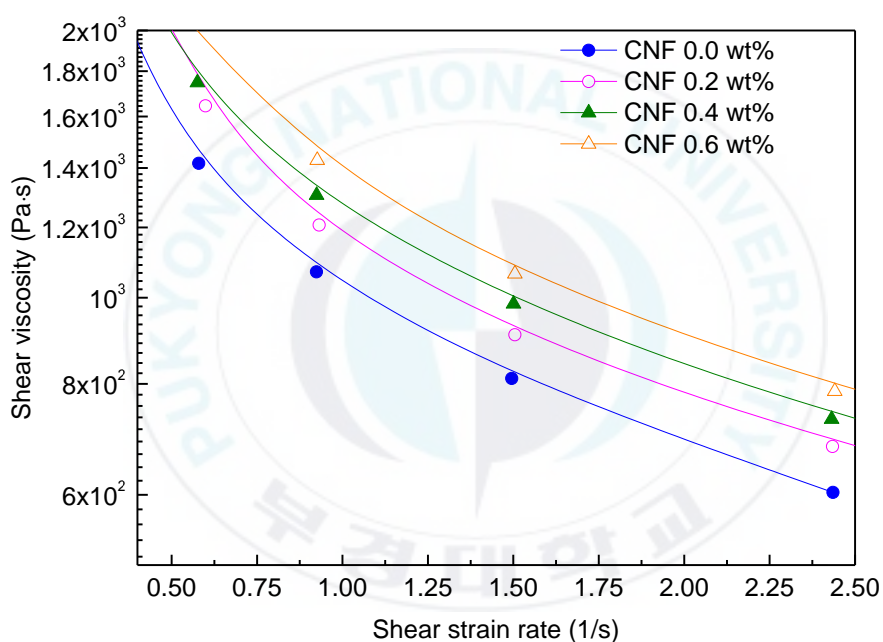


Fig. 29 Shear viscosities of silver paste at different CNF concentration

By plotting shear strain rate versus shear stress, the appearance yield stress of silver paste can be examined, as shown in Fig. 30. The silver pastes containing CNF are known to have higher yield stress at higher incorporation concentration. At 0, 0.2, 0.4 and 0.6 wt% CNF concentrations have clearly defined yield stress of 677.5, 812.7, 813.83 and 818.10 Pa, respectively, because of the interaction between CNF are large enough to exist 3D-network structure and generated yield stress [53].

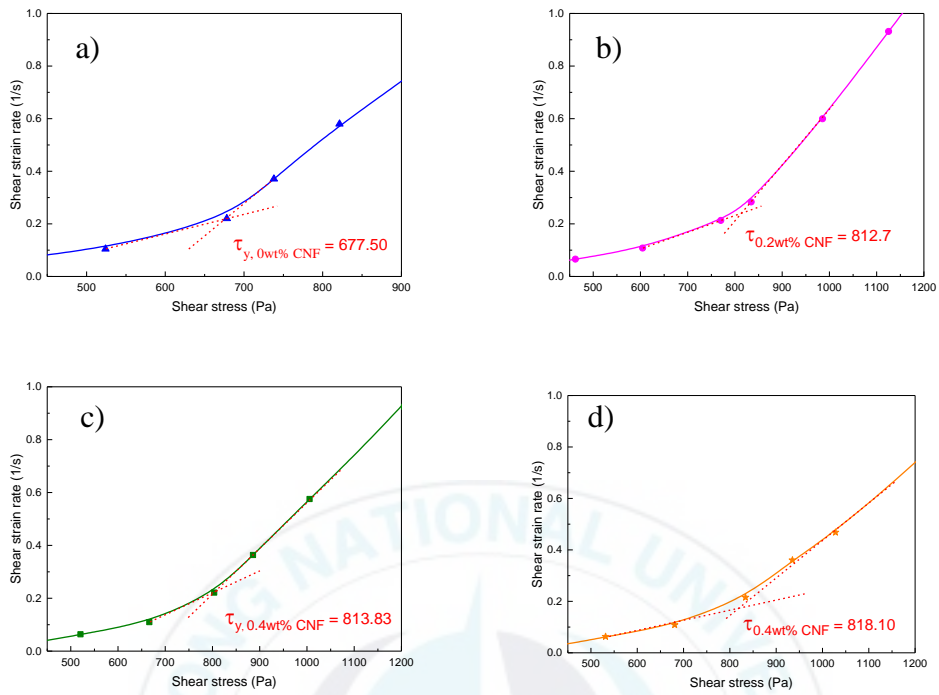


Fig. 30 Yield stress of silver paste a) 0 wt% CNF, b) 0.2 wt% CNF, c) 0.4 wt% CNF and d) 0.6 wt% CNF

4.3 The effect of CNF on silver paste consumption

Currently, the most important cost factor for solar cell processing is silver paste consumption. Cell manufacturers are putting a good deal of effort into the reduction of silver paste usage.

In order to reduce the error from the small nozzle in diameter, three kinds of silver paste at 0, 0.2 and 0.4 wt% CNF were dispensed through 100 μm nozzle in diameter with screw pumping of 50rpm at pressure of 0.45MPa. The silver pastes were dispensed 2 min for 3 times to calculate the average amount of silver paste.

Due to the high viscosity of silver paste, the silver paste consumption shows an inverse proportion with CNF concentration, as shown in Fig. 31. For this condition, the silver paste was consumed by 53.91, 39.72 and 30.67 mg/min at 0, 0.2 and 0.4 wt% CNF, respectively. The less consumption can reduce the production cost of silver powder which is an expensive material. However this reduction of silver pastes usage leads to thinner finger electrodes and results in higher power losses.

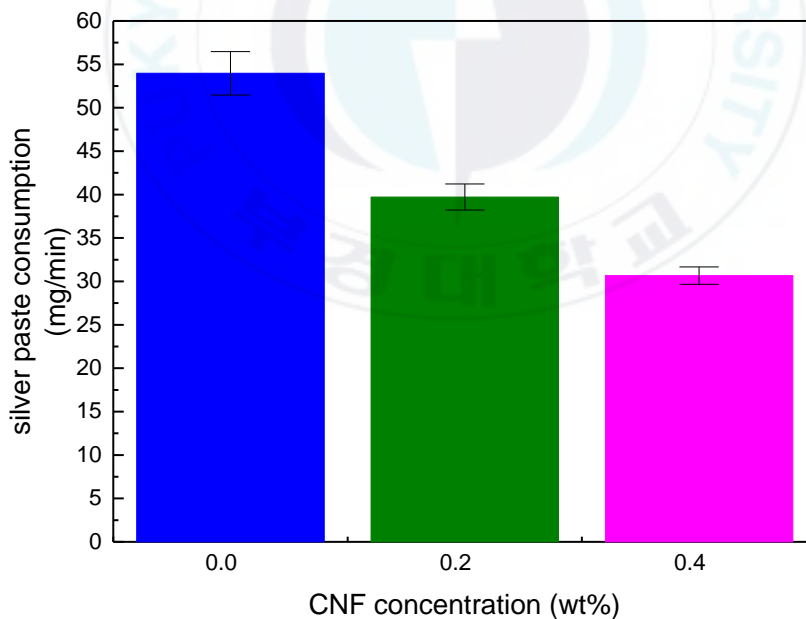


Fig. 31 The influence of CNF on silver paste consumption

4.4 The effect of CNF on elongational property and finger line width

Due to the elongational property, it was found that the increase of CNF weight fraction in silver paste resulted in the reduction of the average width of finger electrodes. The dispensed in-house developed silver paste containing CNF could elongate from the nozzle tip to the substrate without line breakage (Fig. 32b). On the other hand, the discontinuously dispensed line of in-house developed silver paste without CNF was clearly observed before reaching to the substrate (Fig. 32a). However, the increase of CNF at the certain point (0.5 wt% CNF) shows some swinging behavior of silver paste (Fig. 32c).

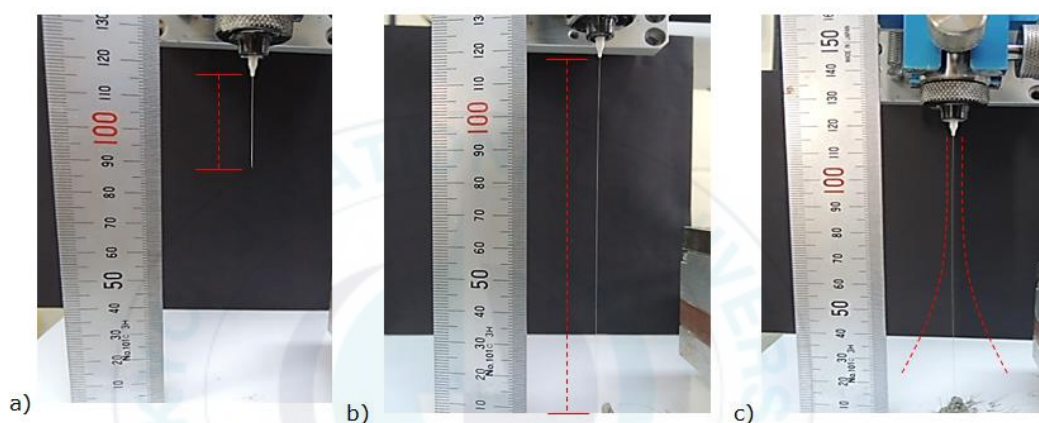


Fig. 32 The elongational property of In-house developed silver paste a) without, b) with 0.2 wt% CNF and c) with 0.5 wt% CNF

A further confirms the elongational property of silver paste containing CNF, the commercially available silver pastes without and with 0.2 wt% CNF were compared by dispensing out of the 50 μm nozzle in diameter at different screw rpm. The elongational of CNF increased the yield of continuous line (Fig. 32a). The disrupt line was found only at start and end point (Fig. 33e); the continuous lines were calculated to be 19% at screw pumping of 30rpm. As the screw pumping was increased over 30 rpm, the continuous lines of dispensed commercially available silver paste containing 0.2 wt% CNF were obviously seen without line breakage (Fig 33f and 33g). On the other hand, the dispensed commercially available silver paste without CNF at screw pumping of 30rpm shows the discontinuity line for whole wafer in which, the continuous line was calculated to be 13% (Fig. 33b). The disrupt lines could also be found when dispensed at screw pumping of 40rpm and 50rpm as 21% and 1%, respectively. However 100% continuous lines were achieved at screw pumping over than 50rpm.

According to this experiment, we can conclude that the addition of CNF increase the elongational property of silver paste to construct narrower finger electrodes.

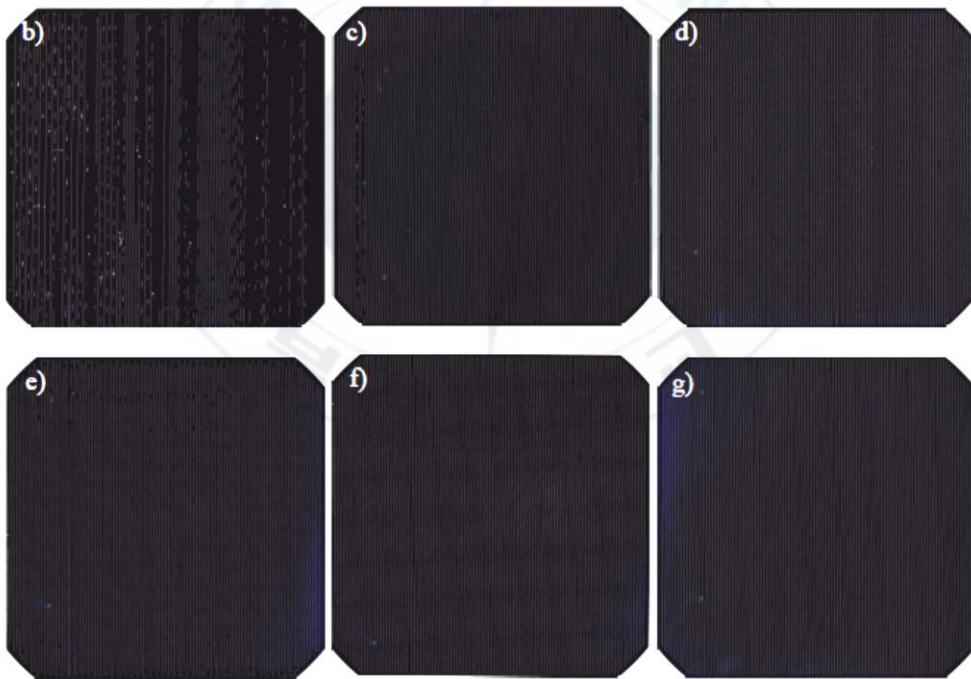
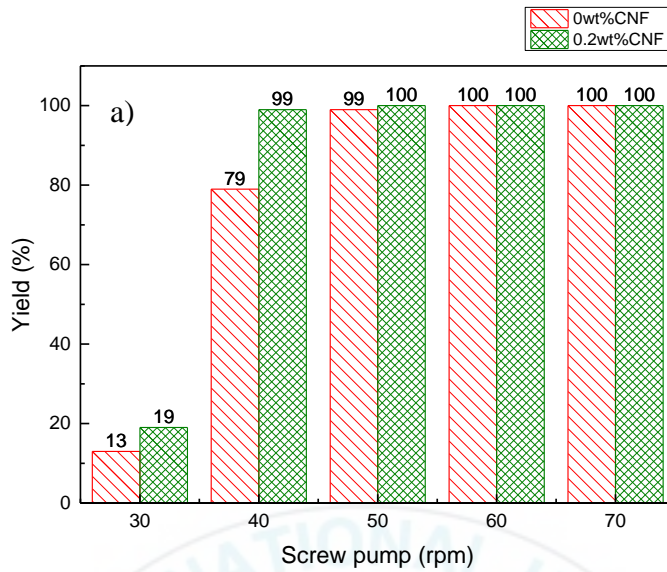


Fig. 33 a) The yield of continuous line at screw pumping of 30, 40, 50, 60 and 70rpm b), c) and d) dispensed commercially available silver paste without CNF at the screw pumping of 30, 40 and 50rpm and e), f) and g) dispensed commercially available silver paste containing 0.2 wt% CNF at screw pumping of 30rpm, 40 and 50rpm, respectively.

In the term of dispensing printing, the rapidly recover yield stress is necessary to construct narrow finger electrode. Due to the high shear stain rate, the silver paste rapidly decreases the viscosity and passes through the nozzle. For the ideal shear thinning behavior of silver paste, the shear stain rate is no longer applied to the silver paste when the silver paste is push out of the nozzle. The yield stress can be recovered at a zero strain rate. Finally, the spreading of the silver paste is prevented.

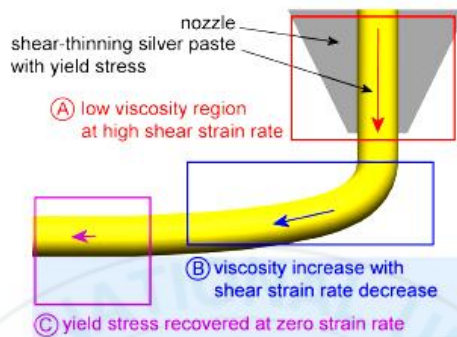


Fig. 34 The rheological behavior of the shear thinning silver paste with the recovery of yield stress by dispensing printing [26]

In this case, as increase the screw pumping rpm, the pastes with a good rheology decrease sharply, the silver pastes can flow rapidly through the nozzle. However they don't have enough time to recover their yield stress. Thus, the finger electrode would spread out when the silver pastes contact with the solar cell wafer (Fig. 35). Nevertheless, the low shear stain rate as screw pumping of 30rpm of dispensed commercially available silver paste without CNF could not construct continuous finger line, as show in Fig.33b) and 33c) because lower stretchable of silver paste.

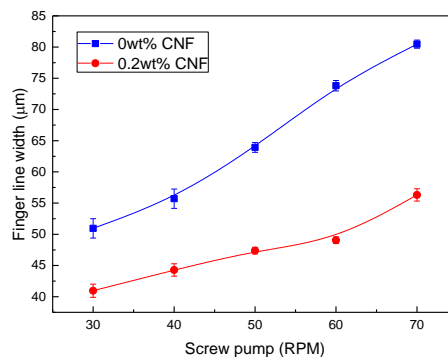


Fig. 35 The effect of finger line width on screw pumping

In this study, the different CNF concentrations were incorporated into the commercially available silver paste to investigate the influence of CNF on finger line width.

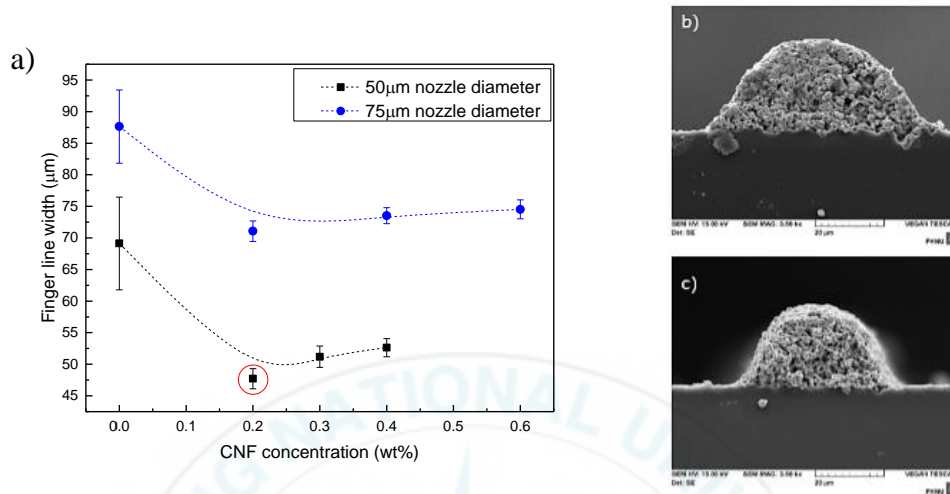


Fig. 36 a) The effect of CNF concentration on finger line width by dispensed on monocrystalline silicon solar cell and SEM image of dispensed finger electrode at b) 0 wt% CNF and c) 0.2 wt% CNF through 50 µm nozzle in diameter

After pre-filtered commercially available silver pastes with 1000 and 1550 mesh for dispensed through 75 µm and 50 µm nozzle diameter, respectively, the silver pastes were dispensed at room temperature. Table 5 shows the dispensing condition which indicated that the incorporation of CNF wasn't affected on the printing condition, but it was strongly affected on the reduction of the printed line width.

As shown in Fig. 36a), the incorporation of CNF in commercially available silver paste, resulted in reduction of dispensed finger electrode width. The average dispensed finger electrode width was achieved to be 87.6, 71.1, 73.5 and 74.5 µm at 0, 0.2, 0.4 and 0.6 wt% CNF through 75 µm nozzle in diameter, and 70.2, 47.72, 51.19 and 52.6 µm at 0, 0.2, 0.3 and 0.4 wt% CNF through 50 µm nozzle in diameter, respectively.

Table 5 Printing condition

Condition Name	Nozzle diameter (μm)	Screw rpm (rpm)	Printing speed (mm/s)	Pressure (MPa)	Nozzle high (mm)
Commercially silver paste	75	40	100	0.45	45.6
	50	60	100	0.485	45.6
Commercially silver paste +0.2 wt% CNF	75	30	100	0.45	45.6
	50	70	100	0.485	45.6
Commercially silver paste +0.3 wt% CNF	50	70	100	0.485	45.6
Commercially silver paste +0.4 wt% CNF	75	40	100	0.45	45.6
	50	70	100	0.485	45.6
Commercially silver paste +0.6 wt% CNF	75	40	100	0.45	45.6

The electrode width was achieved finer than $50\ \mu\text{m}$ by incorporated 0.2 wt% CNF in the commercially available silver paste which dispensed out of the $50\ \mu\text{m}$ nozzle in diameter. It is noteworthy that the average width of finger electrodes did not further decrease above a certain weight fraction of CNF in silver paste. Moreover there was some clogging problem for small nozzle diameter when the CNF concentration was increased above 0.4 wt%.

Fig. 36b) and 36c) demonstrates that the finger electrodes containing CNF can construct higher aspect ratio than the silver paste without CNF. Moreover there is no necking of electrode. In this study, the geometric width was assumed to be optical finger width. Therefore geometrical shading was defined by the ratio of optical finger width to finger spacing [54, 55]. To demonstrate the shading losses of solar cell, the printed line widths at 0 wt% and 0.2 wt% CNF through $50\ \mu\text{m}$ nozzle in diameter were compared. The 78 fingers with a width of $70\ \mu\text{m}$ shaded about 3.5% of the $15.6 \times 15.6\ \text{cm}^2$ by sized of solar cell wafer compared to 2.4% for the solar cell with $48\ \mu\text{m}$ wide fingers

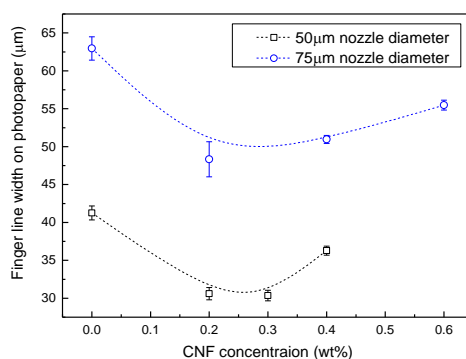


Fig. 37 The effect of CNF concentration on finger line width by dispensed on photopaper

This research also studied the influence of surface condition on finger line width. The silver paste spread would be limited by dispensed on photopaper due to the clay composite coating which is a highly absorbance materials [56]. When the silver pastes were dispensed on photopaper, solvent was absorbed and prevented the diffusion of paste away from the contact point (Fig. 37b). On the other hand, there are no absorbance materials coating on silicon solar cell wafer, resulted in wider line width (Fig. 37a). In order to determine the limit of elongational property of silver paste, the dispensed lines width on photopaper of commercially available silver paste were compared to the dispensed lines on mono-crystalline silicon solar cell with the same weight fraction of CNF.

As expected, the electrodes constructed by dispensing process on photopaper shows reduction of line width compared to the line width on mono-crystalline silicon solar cell wafer (Fig. 25). The dispensed line width through 50 μm nozzle in diameter was achieved as narrow as 30 μm in average at the concentration of 0.2 wt% CNF. Based on an experiment resulted, we still have room for constructing ultra-fine electrodes.

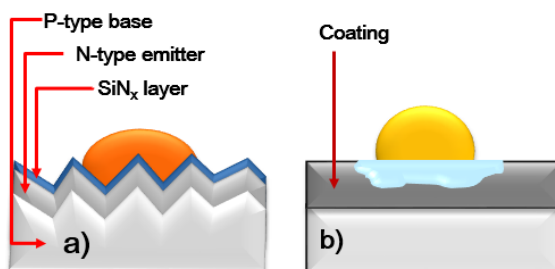


Fig. 38 The influence of surface condition of a) silicon solar cell wafer and b) photopaper on finger line width

4.5 The effect of CNF on thermal property

In order to confirm the reaction between CNF and other ingredients in silver paste, thermo gravimetric analysis (TGA) was investigated. Fig. 39 shows the TGA results of pure CNF, pure glass frit (GFV2172), commercially available silver paste and the mixture of GFV2172-CNF, Ag-GFV2172-CNF, and commercially available silver paste-CNF in the air at 1:0.15, 1:1:0.15 and 20:0.5 weight ratios, respectively. The pure glass frit powder has almost no weight loss due to the formation of metal oxide. For the weight of GFV2172-CNF and Ag-GFV2172-CNF mixture is remain over than 95% which demonstrate that there is no reaction between CNF and other inorganic ingredients.

According to the TGA of pure CNF, could not completely thermal decompose even at high temperature above 800°C. By compare the mixture of CNF in commercially silver paste, it is indicated that there is remaining of CNF in silver pate after co-firing process. This characteristic was affected to the electrical properties of silver electrodes.

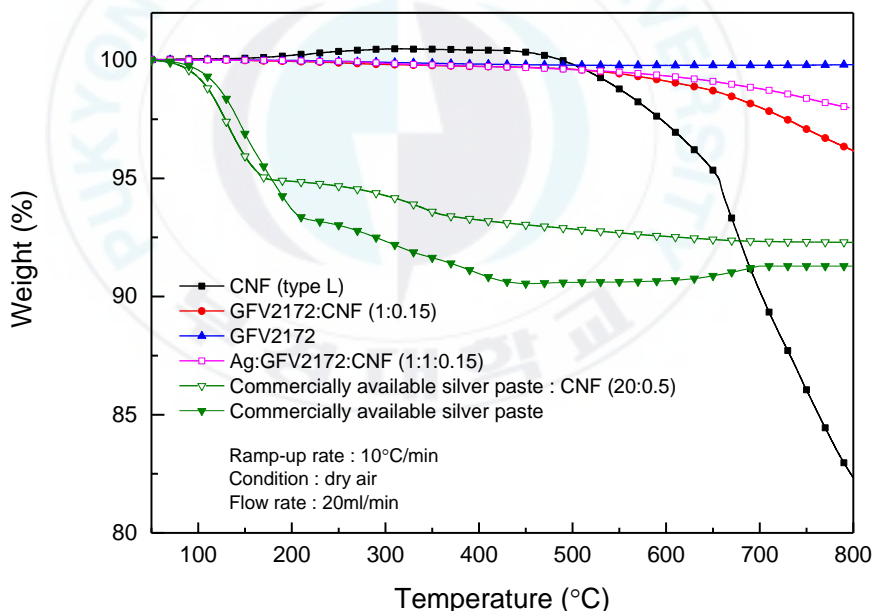


Fig. 39 TGA results of pure CNF, pure GFV2172, commercially available silver paste, GFV2172-CNF (1: 0.15), Ag-GFV2172-CNF (1: 1: 0.15) and mixture of commercially available silver paste – CNF (20: 0.5) in weight ratio

4.6 The effect of CNF on electrical properties

A typical co-firing profile of a crystalline silicon solar cell is shown in Fig. 40. The first step, the organic compounds are burnt out at temperature about 400°C. At temperature about 800°C, the contacts are formed. Finally, the solar cell wafer is cooled down.

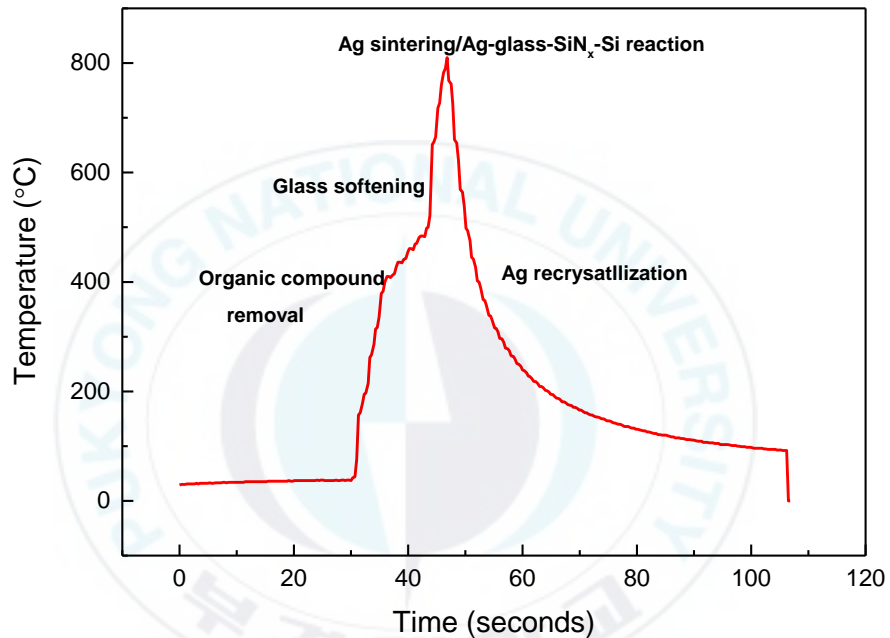


Fig. 40 The temperature profile of a crystalline silicon solar cell in RTP

During firing process, glass frit which contains lead oxide (PbO) is melted and etched the SiN_x layer as antireflection coating layer to introduce the conductive particle (silver powder) contact with the emitter layer. There are two possibilities of current transportation mechanism. First, the current is transport via the silver crystallites which direct contact between the silicon substrate and silver particle. Silver crystallites are growth and distributed over the surface [57, 58]. Due to the dissolve of silver in glass layer, the second probability is current flowing via the nano-silver colloids in glass layer [59, 60] (see in Appendix B).

4.6.1 The effect of CNF on contact resistivity

In case of silver paste containing CNF, the electrical properties were affected by the increase of CNF concentration. The concept of contact mechanism through CNF integration is illustrated in Fig. 38 which based on the nanostructure of CNF. The network structure of CNF (Fig. 28) blocked the molten glass frit to etch SiN_x layer and make less contact between silver electrode and crystalline silicon solar cell wafer (Fig. 42a and 42b), resulted in increase of contact resistivity (Fig 41).

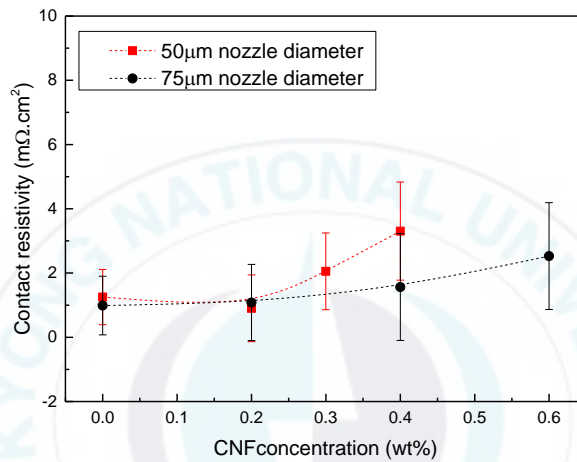


Fig. 41 The statistical analysis of CNF concentration on contact resistivity

The contact resistivity is slightly increased with increase the weight fraction of CNF by dispensed silver paste through 75 μm nozzle diameter, but it became more effective when the finger electrode width was narrower. The contact resistivity of 0, 0.2, 0.3 and 0.4 wt% CNF by dispensed through 50 μm nozzle diameter was 1.213, 0.902, 2.054 and 3.304 mΩ.cm², respectively.

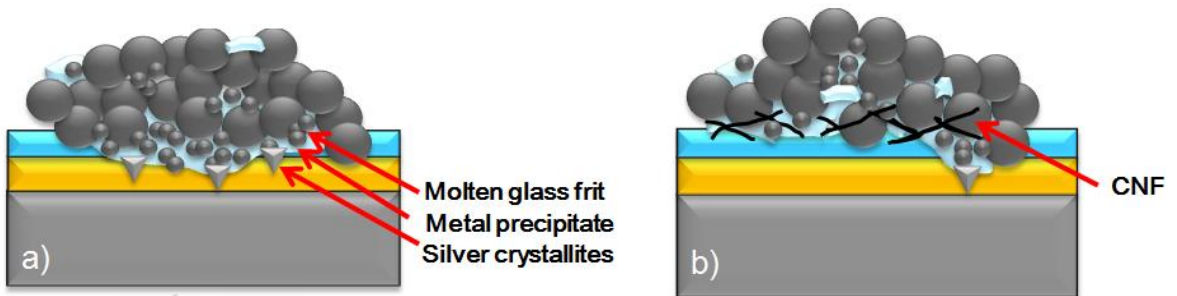


Fig. 42 The mechanism to form contact between a) silver paste without and b) with CNF

In order to understand the behavior of CNF in silver electrode, the law of filtration [61, 62] was considered. The complete blocking filtration law (Fig. 43c) is described as an extreme situation. Each particle that reaches the medium surface participated in blocking process that results in sealing of a pore. The further particles are not superimposed on those already deposited, the medium surface becomes blocked and is no longer available to support the flow of filtration.

The intermediate blocking filtration law (Fig. 43b) considers that first coming particles medium will block a pore of filter medium, but later particles will come and rest on deposited particles to form bridging. This phenomenon occurs when the pore sizes are smaller than particles with low to medium concentration of solid in feed.

A less several blocking process is described by the standard blocking filtration law (Fig. 43a). It is assumed that the pore volume decrease proportionally with the filtrate volume produced, due to deposition of particles on the walls of a pore. In this case all pores are assumed to be the same length and diameter, and the decrease in pore volume is directly related to a decreased in pore cross-sectional area.

The standard blocking law is the main approach to depth filtration that describes continuous accumulation of particles in medium. The combination of blocking and bridging causes cake filtration. Both cake formation and pore blocking can occur in the intermediate blocking mechanism.

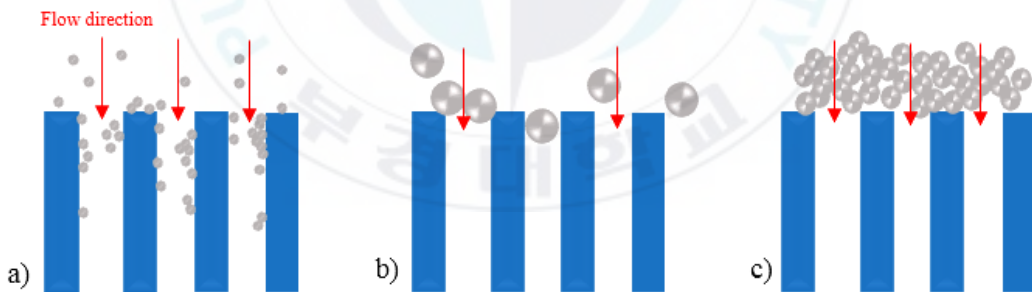


Fig. 43 Mechanism of filtration of a) the complete blocking filtration law b) the intermediate blocking filtration law and c) the standard blocking law

In the case of fibrous or woven media which is heterogeneous structure with non-uniform size and irregular geometry. The network structure effects on particles deposition and packing of filter cake at the medium surface. When the yarn of multifilament fabric is made up from many smaller fibers that are twisted together, the geometries of fibers a yarns that make up a multifilament fabric are very complex.

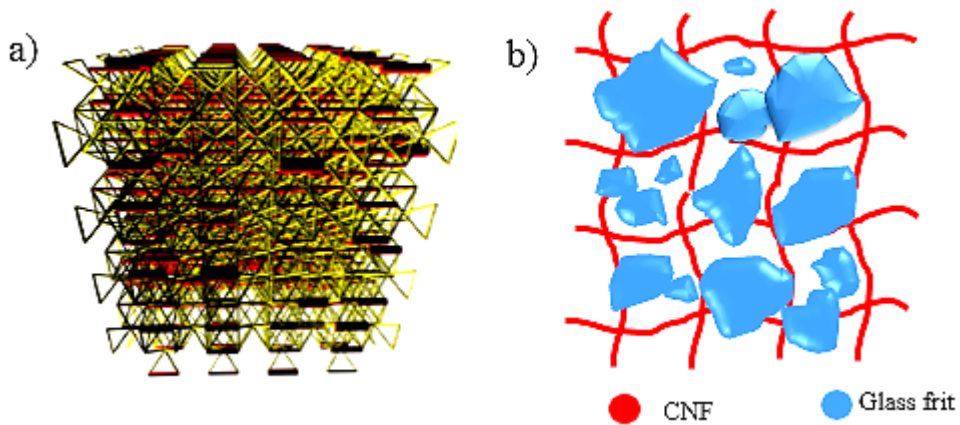


Fig. 44 Schematic presentation of a) pore network model [63] and b) the effect of CNF on penetrability of glass frit [64]

In this study, CNF filter medium is considered to be network pore model with different pore shape and non-uniform is shown (Fig. 44a). Therefore the increase of CNF concentration reduced the degree of medium openness or porosity, resulted in lower penetrability of glass frit to solar cell surface (Fig. 44b). To further confirm this hypothesis, the mixture of GF and CNF was prepared. As shown in Fig. 45, pure glass frit particles are loosely packed while porosity is reduced by incorporated CNF in the mixture.

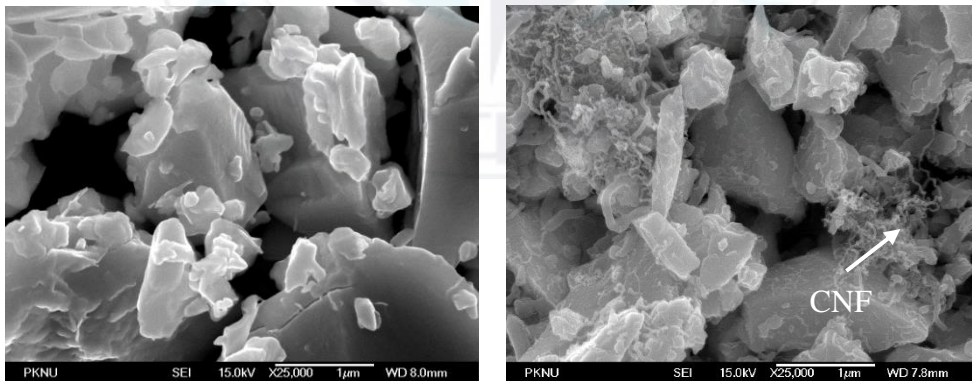


Fig. 45 FESEM image of a) pure glass frit and b) mixture of glass frit to CNF at 1:1 volume ratio (1:0.15 weight ratio)

However the concentration of CNF at range of 0 to 0.2 wt% did not impact to the contact resistivity in both cases. By compared the contact resistivity of dispensed available silver pastes without and with 0.2 wt% CNF through 50 μm nozzle in diameter at various screw pumping from 40 to 70rpm, it was found that there is no significant difference between screw pumping of 40 and 50rpm for commercially available silver paste without CNF and 70rpm for available silver paste containing 0.2 wt% CNF, the contact resistivity was measured to be 0.211, 0.208 and 0.219, respectively. This implies that contact resistivity depended on the finger width since the contact area is inversely proportional to the contact resistivity. As contact area increases by increasing the width of finger electrode, the contact resistivity decreases [65, 66, 67].

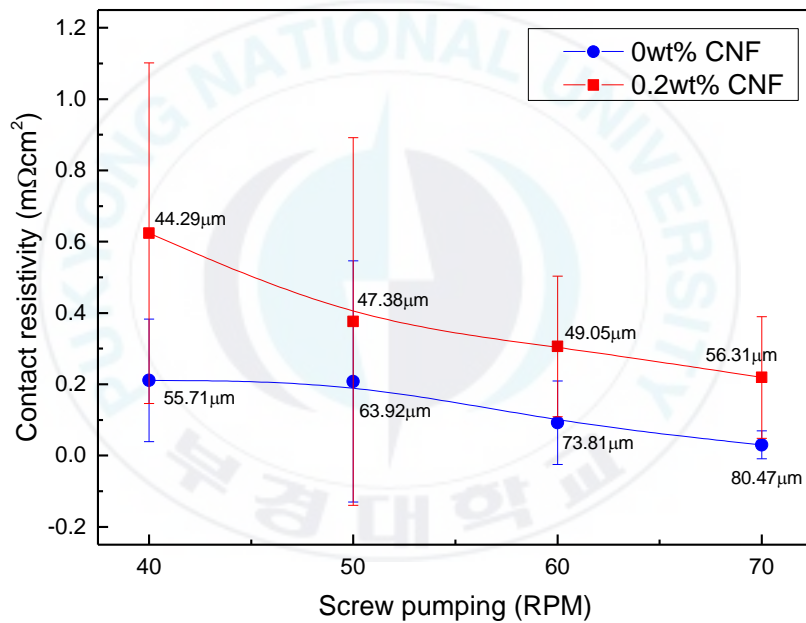


Fig. 46 The contact resistivity variation with the screw pumping rpm for the finger electrodes which dispensed through 50 μm nozzle in diameter

4.6.2 The effect of CNF on resistivity

The significant potential for further increase cell efficiency is front side metallization techniques. Beside of the minimization of shading loose by reduction of electrode, high electrode conductivity is also required to transport the current possible out of the solar cell wafer without the electrical losses. The calculation the configuration of rectangular slice for resistivity measurement is described in detail in Appendix C.

Fig. 47 demonstrates the resistivity of commercially available silver paste with various CNF concentrations. It was observed that the resistivity gradually enhances with increase CNF concentration. The electrical transfer was impeded due to the residual of CNF in silver electrode. The calculated resistivity at room temperature of 0, 0.2, 0.4 and 0.6 wt% CNF was recorded to be 9.6, 9.79, 9.95 and 10.6 $\mu\Omega$.cm, respectively, which approximately 16 times higher than bulk silver [68]. However, the electrical properties decrease could not degrade the solar cell performances. By trade-off between finger line width and contact resistivity, the appropriate CNF concentration is 0.2 wt%.

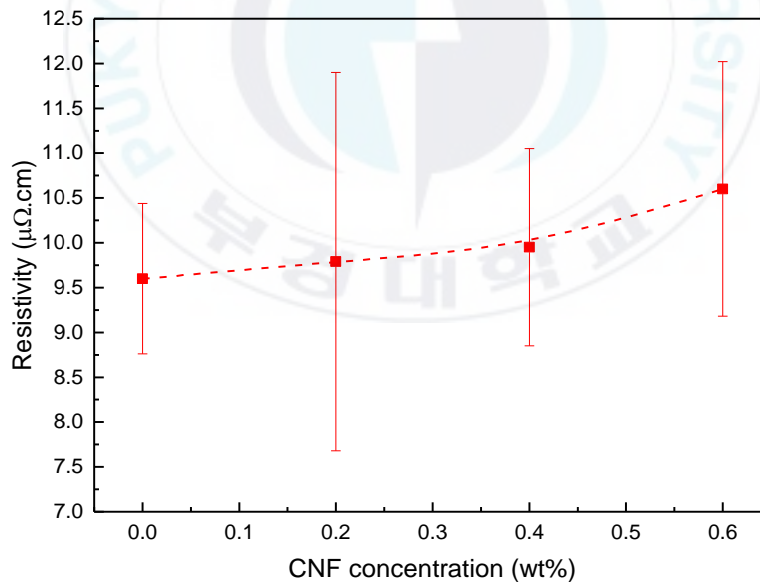


Fig. 47 The effect of CNF on resistivity

4.7 The effect of CNF on cell efficiency

The solar cell wafer at least 5 wafers of 3 groups for commercially available silver paste without CNF and commercially available silver paste wafer containing 0.2 wt% CNF were measured the cell efficiency at different firing temperature.

Table 6 The comparison between average cell efficiency of solar cells fabricated by commercially available silver paste without CNF and commercially available silver paste with 0.2 wt% CNF at ramp-up rate of 100°C/s (see more detail in Appendix D)

Name	Peak firing Temperature (°C)	V _{oc} (mV)	I _{sc} (A)	J _{sc} (mA/cm ²)	FF (%)	Eff (%)	R _s (mΩ)	R _{sh} (Ω)
Without CNF	790	634.4	8.5	35.6	80.2	18.10	6	17.6
With 0.2 wt% CNF	790	636.0	8.6	36.0	79.9	18.32	6	82.4
Without CNF	810	635.60	8.5	35.9	80.2	18.18	6	14.2
With 0.2 wt% CNF	810	635.67	8.6	35.9	80.0	18.28	6	37.8
Without CNF	830	635.0	8.5	35.5	79.4	17.92	7	8.6
With 0.2 wt% CNF	830	635.6	8.6	35.9	79.5	18.14	7	9.9

Fill Factors above 78.5% implied a good printing performance as well as contacting behavior of dispensed silver paste in all groups. On the other hand, the slightly decrease in FF of 0.2 wt% CNF cells which is mainly due to a significantly increase the series resistance of electrodes.

A reduction of printed electrode width increased short circuit current density (J_{sc}) values of dispensed metal contact due to substantially lower shading losses. Since the incorporation of 0.2 wt% CNF in silver paste enhanced the defect free printability of finger electrodes which is a main focus on industrial application. Additionally the incorporation of CNF in commercially available silver paste also improved the shunting problem, because of the CNF prevented the aggressive glass frit to etch away SiN_x and emitter layer, as discuss in Appendix E.

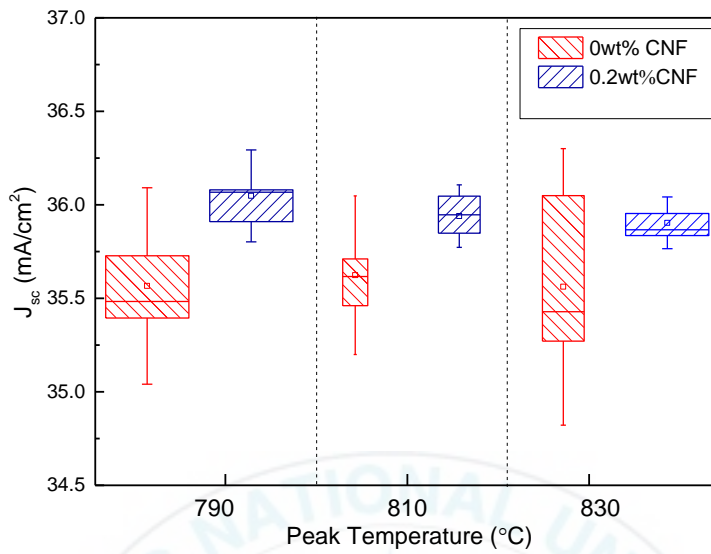


Fig. 48 The J_{sc} of commercially available silver paste with and without CNF at different peak temperature

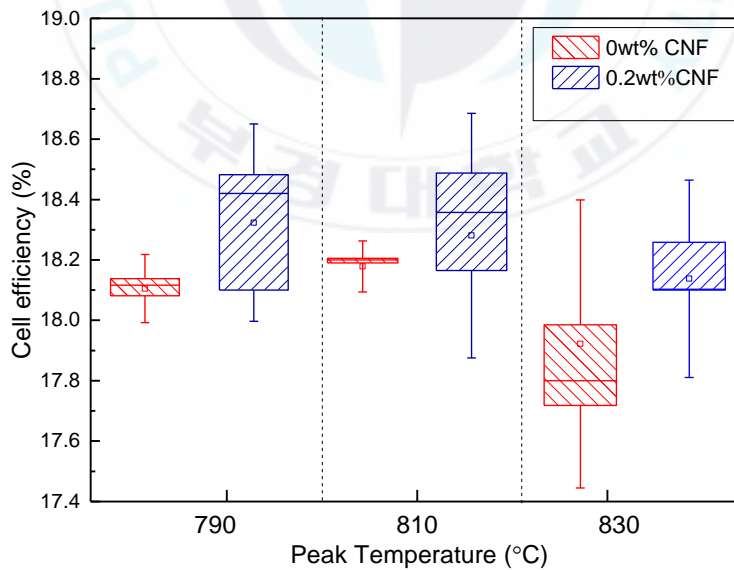
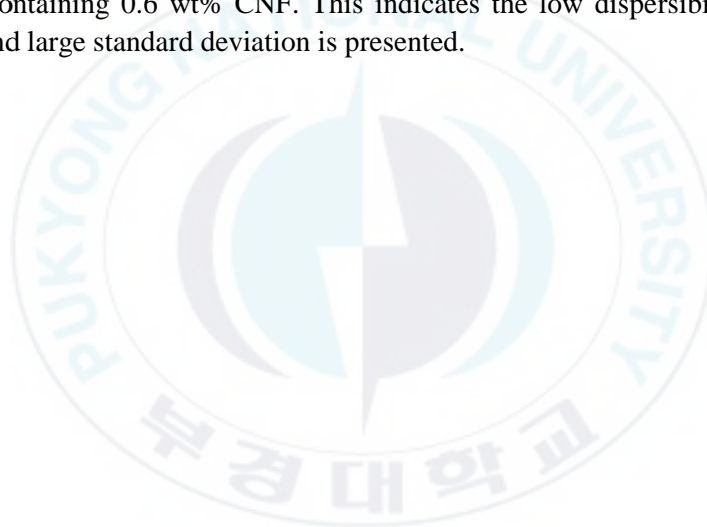


Fig. 49 The efficiency of commercially available silver paste with and without CNF at different peak temperature

Consequently, the resulting of average efficiencies show a significant increase of all dispensed commercially available silver paste containing 0.2 wt% CNF cells compared to the dispensed cells without CNF, which improved +0.22, +0.10 and +0.22% at peak temperature 790, 810 and 830°C, respectively. The best cell efficiency exhibited a J_{sc} of 36.06 mA/cm² and an energy conversion efficiency of 18.52% for commercially available silver paste contained 0.2 wt% CNF which was confirm by KIER (Korea Institute of Energy Research). As the temperature increases, the bowing of the wafer or microcrack in the wafer might occur, large defect of wafer leading to an increase in surface recombination which causes an increase the leakage current [44], resulted in lower cell efficiency. Therefore the appropriate peak firing temperature is in the range of 790 to 810°C.

Even the CNF is better than MWCNT in term of dispersibility, the big void also be found in the firing finger electrode which dispensed from commercially available silver paste containing 0.6 wt% CNF. This indicates the low dispersibility of CNF in silver paste and large standard deviation is presented.



5. Conclusion

In order to improve the defect free printability and minimize shading losses, the addition of CNF in silver paste was successfully approach. A continuous printing process was applied at printing speed 100mm/s with single-pass dispensing and also 26% less silver paste consumption, which can be scaled for an application in cell production.

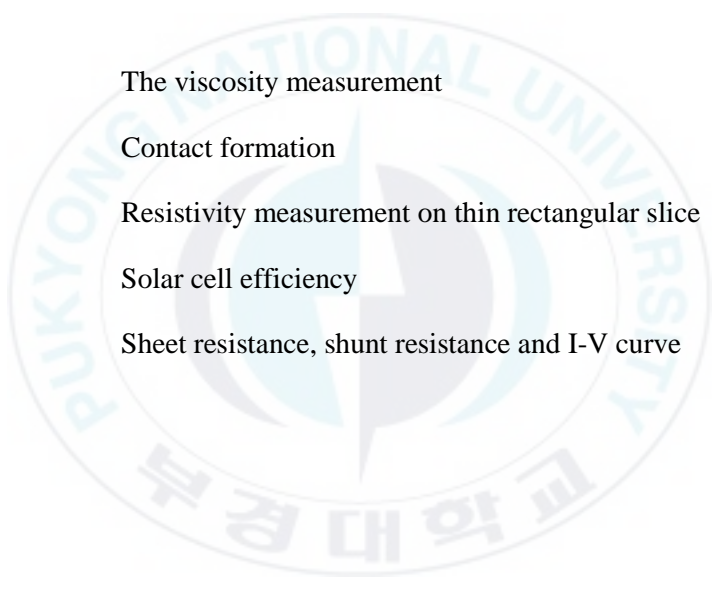
The line width of electrode was narrower by increase the weight fraction of CNF due to the elongational property. The homogeneously dispensed finger electrode width on crystalline silicon solar cell with a 50 μm nozzle diameter was achieved as narrow as 47.72 μm in average by adding 0.2 wt% CNF, which was narrower than the width of silver paste without CNF by 31%.

The maximum efficiency of solar cell prepared by commercially available silver paste containing 0.2 wt% CNF exhibited 18.52%. The temperature profile during the co-firing process does influence to the produced cells. The commercially available silver paste containing 0.2 wt% CNF shows an efficiency improved +0.22, +0.10 and +0.22% at peak temperature 790, 810 and 830°C, respectively, in comparison to the commercially available solar cell without CNF. Since the microcrack generation leading to an increase in surface recombination, resulted in lower efficiency at high temperature.

Appendices

The treatments in Appendices A to D are neither rigorous nor complete; they are intended to be illustrative and given the types of theories involved or some experiment data for supporting the dissertation.

- Appendix A. The viscosity measurement
- Appendix B. Contact formation
- Appendix C. Resistivity measurement on thin rectangular slice
- Appendix D. Solar cell efficiency
- Appendix E. Sheet resistance, shunt resistance and I-V curve



Appendix A

Viscosity measurement

Functional principle:

The substance which needs to be measured the viscosity is filled in the gap between rotor and container of system. The motor is rotated at a known speed (v). Due to the viscosity of fluid, a resistance is exerted to this rotational movement as a torque value (τ) which applied on the viscometer measurement [69]. The measurement principle is shown in Fig. A-1.

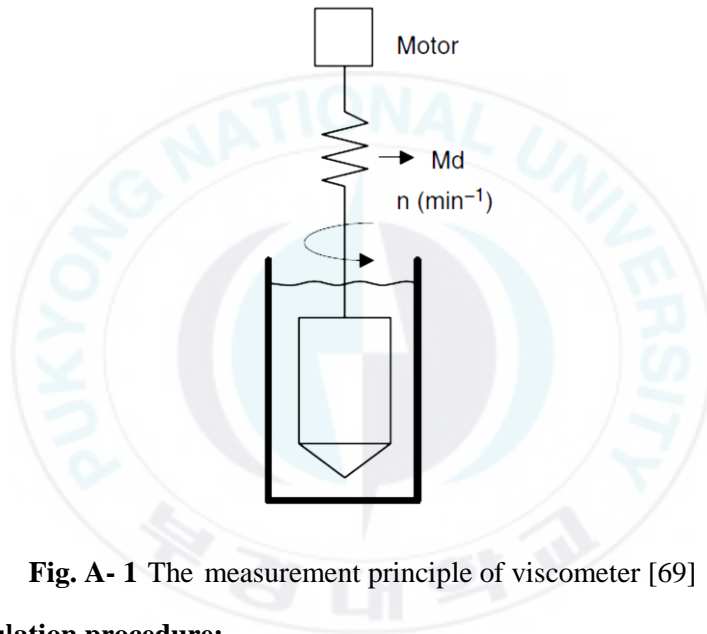


Fig. A- 1 The measurement principle of viscometer [69]

Calculation procedure:

Viscosity (μ) describes by definition the relationship between shear strain rate (γ') and shear stress (τ).

$$\mu = \frac{\tau}{\gamma'} \quad [\text{A-1}]$$

Starting with the measured values for “torque (τ)” and “speed (V)”, the geometric characteristics of the various sensor systems are accounted for in the calculation by the system factors; the equation [7] can now be supplemented as follows:

$$\mu = \frac{F \cdot \tau}{M \cdot V} \quad [\text{A-2}]$$

The further steps in the calculation process are not illustrated here, but they result in the following equations:

Cylinder systems:

$$F = \frac{0.01}{2\pi LR_i^2} , M = \frac{\pi}{15} \cdot \frac{R_a^2}{R_a^2 - R_i^2} \quad [A-3]$$

Plate-cone systems:

$$F = \frac{0.03}{2\pi R_i^3} , M = \frac{\pi}{30\alpha} \quad [A-4]$$

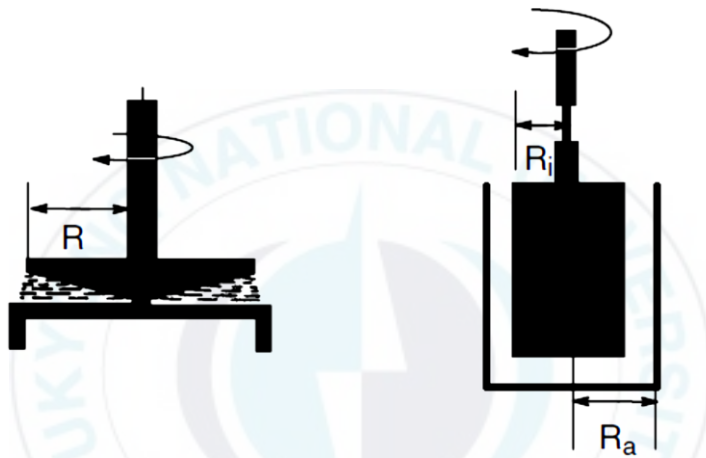


Fig. A- 2 Schematics of cone-plate and plate-plate model [70]

Where:

R_i is radius of the rotor (inner cylinder or cone) (m), R_a is radius of the cup (outer cylinder) (m), L is rotor length (inner cylinder) (m), α is angle of rotor or cone (rad), τ = torque (N.cm) and n = rotor speed (1/min) [70].

Flow properties regarding viscosity behavior:

A few basic phenomena have been summarized below in order to enable a better understanding of the flow properties. They can be categorized in accordance with the behavior of viscosity, as shown in Table A-1.

Table A- 1 The categorized of viscosity behavior

Name	Properties	Graph [70,71]
Newtonian	The viscosity does not change with shear stain rate and shear stress.	<p>The graph plots Shear Stress τ on the vertical axis against Rate of Shear, du/dy on the horizontal axis. It shows four curves: Bingham plastic (a straight line starting from a positive y-intercept), Pseudo plastic (a curve that starts at the origin and its slope decreases as shear rate increases), Newtonian fluid (a straight line starting from the origin), and Dilatant (a curve that starts at the origin and its slope increases as shear rate increases).</p>
Pseudoplastic/ Shear thinning	The viscosity decreases with increase shear stain rate and shear stress.	
Dilatant/ Shear thickening	The viscosity increases with increase shear stain rate and shear stress.	
Bingham plastic	<ul style="list-style-type: none"> - Substances start flowing after applied at a certain force (shear stress) - The yield point strongly depends on external parameters like temperature and change rate of the acting force. 	
Thixotropix	<ul style="list-style-type: none"> - Non-Newtonian behavior in which the viscosity decreases with increase shear rate. - The substance will eventually regain their viscosity after removal the load. 	<p>The graph plots Shear Stress τ on the vertical axis against Shear Rate $\dot{\gamma}$ on the horizontal axis. It shows three curves: Bingham (a straight line starting from a positive y-intercept), Thixotropic (a curve that starts at the origin and its slope decreases as shear rate increases, with a hysteresis loop indicated by arrows), and Rheopectic (a curve that starts at the origin and its slope increases as shear rate increases, also with a hysteresis loop indicated by arrows).</p>
Rheopectic	<ul style="list-style-type: none"> - Non-Newtonian behavior in which the viscosity decreases with increase shear rate. - The substance will eventually regain their viscosity after removal the load 	

Appendix B

Contact formation

Front contact formation and current transportation

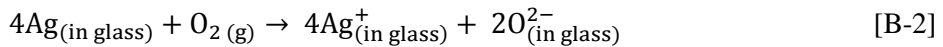
Typically silver paste consists of silver powder, glass frit, solvent, organic blinder, rhepological modifier and other additives. Glass frits is a key to promote the contact formation between n-type emitter of silicon solar cell and silver electrode and also affects the metal powder sintering kinetics.

Normally a lead oxide (PbO) glass is the most important ingredients. Other additives as bismuth, zinc, titanium and aluminium can be added. However the amount and type of glass frit is responsible for an V_{oc} degradation at high temperature since large amounts of the emitter region are dissolved, contaminated and recrystallited [72].

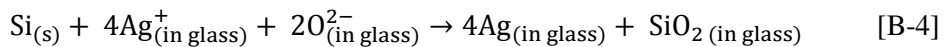
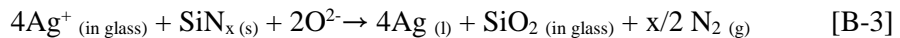
Before forming contact between silver and silicon, the SiN_x is normally used for antireflection coating (ARC) and SiO_2 is used for surface passivation need to be opened. At temperature about 600-700°C, the fluidize glass frit wets the SiN_x surface. The reaction between lead oxide glass frit and SiN_x dielectric layer is given as:



The products of this reaction are liquid lead particle precipitating above silicon wafer. Nitrogen gas (N_2) generates large pores in the glassy layer. At the same time, silver dissolves into the fluidized glass as silver ions through the interaction with oxygen and the sintering of silver powder occurs even though the temperature is kept below the melting temperature of silver due to the eutectic point of Ag-Si. An interaction between silver ions and oxygen in the atmosphere is shown through the follow reaction [73]:



Both oxygen and silver ions dissolve in the molten glass and diffuse toward silicon wafer and then react with SiN_x layer. The etching of SiN_x layer and silicon emitter by glass frit together with silver powder was likely to occur through the following redox reactions:



During cooling stage of firing, silver particles are divided against lead particles due to their phase diagram. Silver precipitates as silver crystallites which shows invert pyramids in Fig. B-1 on the silicon emitter surface. The precipitation of lead in the glass layer are still found in the firing cell because the dissoluble of silver particle in lead.

Fig B-1 shows front contact formation model after co-firing. During the firing process, silver crystallites are growth and distributed over the surface. There are two possibilities of current transportation mechanism. First, the current is transport via the silver crystallites which direct contact between the silicon substrate and silver bulk or current flows through a very thin (<10 nm) glass layer by tunneling. Due to the dissolve of metal in glass layer, another probability is current flowing via that dissolve silver precipitate in glass layer by multi-step tunneling via metal precipitates.

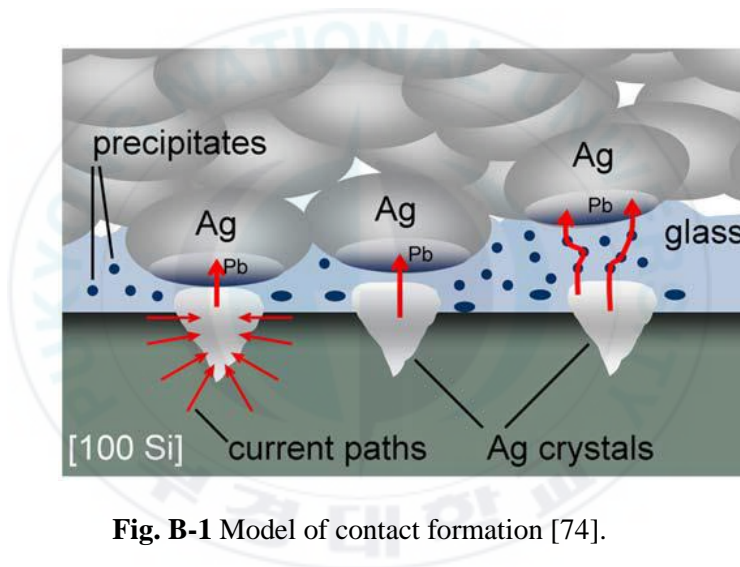


Fig. B-1 Model of contact formation [74].

Since the interaction of earlier molten glass frit and silver particles are allowed for a long period of time, the junction shunting might occur in shallow emitter with low glass transition temperature (T_g) of glass frit due to the providing of a thicker glass layer and larger silver crystallite. Therefore, thin glass layer is desirable for tunneling and a thin glass regions with a large number of very small silver crystallites is appropriate for shallow emitters. Moreover the thin glassy layer demonstrates lower contact resistance [75].

Back surface filed (BSF) formation

The surface passivation layer is required at the front side metallization to minimize surface recombination which is the main impact on I_{sc} and V_{oc} for solar cell [76, 77]. A similar effect is employed at the back surface to reduce the rear surface recombination, called back surface field (BSF) by acts as another PN junction. In the term of optical property, the back contact must reflect with a few absorption, thus it provides effectively to light trapping [78, 79].

The appropriate dopant for back surface field (BSF) is aluminum which is deposited on rare side of silicon substrate by different techniques. After applied high temperature about 577°C , silicon diffused to aluminium and formed layer of aluminium-silicon alloy. As shown in Fig. B-2, the back contact consists of: sintered aluminium particles as a granular region in a matrix of glass, alloyed region due to the Al-Si eutectic and aluminium-doped region that has grown epitaxial on the silicon surface with $10\ \mu\text{m}$ in thickness which shows the interface waviness due to the texturing of cell.

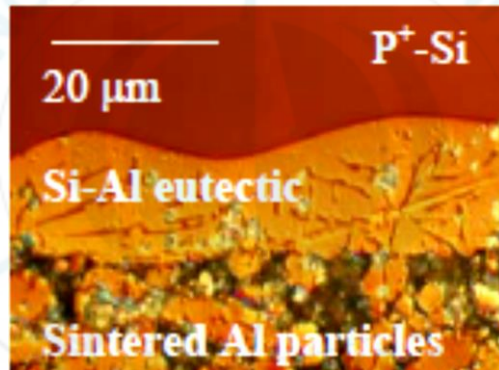


Fig. B-2 Cross-section of back contact region [77]

There are several important factors that affect the BSF quality, one is junction uniformity. The uniformity is controlled by the ramp-up rate. For the slow ramp-up rate, alloying between silicon and aluminium can form a local wetting, results in nonuniformities in BSF layer which include the variation in junction depth, and roughness of p^+ region. For the fast ramp-up rate, the wafer rapidly reaches to the eutectic point. As the co-firing process temperature about 800°C , the molten aluminium readily wets the entire of silicon surface. The uniformity of alloy is promoted, leads to uniform BSF region. At the same time, both junction depth and p^+ region also increase as the BSF alloying temperature increase [80, 81]. However, a cooling rate is desirable for a large P^+ region. Since the different requirement at front and back surface, therefore, the peak firing temperature and ramp-up condition have to optimize.

Appendix C

Resistivity measurement on thin rectangular slice

Geometric factors in four point resistivity measurement:

The electrical resistance (R) of an object is defined as the ratio between voltage (V) that causes current (I) to flow through the object, and the current itself.

In semiconductor resistivity measurements, the most arrangement of the four points is in line. Normally the outer contacts conduct the current and voltage is measured by the inner point as show in Fig. 44.

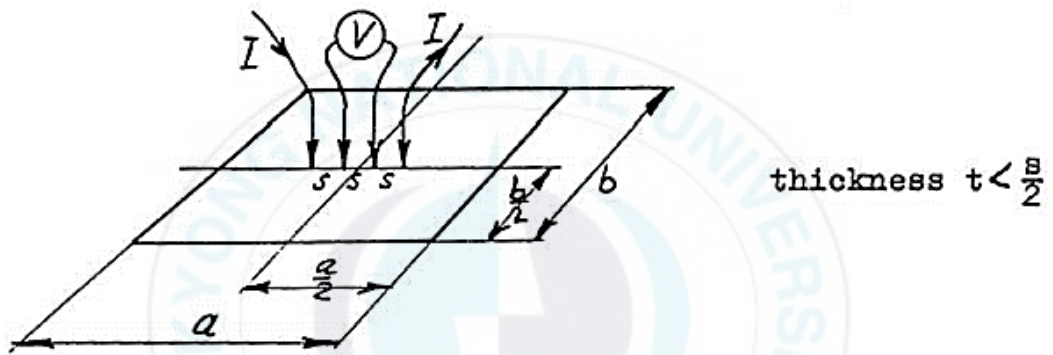


Fig. C- 1 The configuration of rectangular slice for resistivity measurement [82]

The very important task of calculating the correction factor (C) for various shapes and dimensions has been performed during the last decade for most practical applications. The resistivity is given by;

$$\rho = \frac{\pi}{\ln 2} \cdot t \cdot C_1 \left(\frac{b}{s}, \frac{a}{b} \right) \cdot C_2 \cdot \frac{V}{I} \quad [D-1]$$

When ρ is resistivity, t is thickness, V is measured voltage, I is the current passed through the sample, $C_1 \left(\frac{b}{s}, \frac{a}{b} \right)$ is the size correction factor which is shows in Table C₁ and C_2 is the thickness correction factor which show in Table D-1.

Table C- 1 shows the size correction factor (C_1) of Four-Point Probe Resistivity Measurement on thin, rectangular slice

$\frac{b}{s}$	$\frac{a}{b} = 1$	$\frac{a}{b} = 2$	$\frac{a}{b} = 3$	$\frac{a}{b} \geq 4$
1.00			0.2204	0.2205
1.25			0.2751	0.2751
1.50			0.3263	0.3286
1.75			0.3794	0.3803
2.00			0.4292	0.4297
2.50			0.5192	0.5194
3.00	0.542	0.5957	0.5958	0.5958
4.00	0.6870	0.7115	0.7115	0.7115
5.00	0.7744	0.7887	0.7888	0.7888
7.50	0.8846	0.8905	0.8905	0.8905
10.0	0.9313	0.9345	0.9345	0.9345
15.0	0.9682	0.9696	0.9696	0.9696
20.0	0.9822	0.9830	0.9830	0.9830
40.0	0.9955	0.9957	0.9957	0.9957
∞	1.0000	1.0000	1.0000	1.0000

Table C- 2 shows the thickness correction factor (C_2) [83]

$\frac{t}{s}$	C_2
<0.4	1.0000
0.400	0.9995
0.500	0.9974
0.555	0.9948
0.625	0.9896
0.714	0.9798
0.833	0.9600
1.00	0.9214
1.111	0.8907
1.250	0.8490
1.429	0.7938
1.667	0.7225
2.00	0.6336

Appendix D

Solar cell efficiency

Two groups of solar cell were measured the cell efficiency at different peak firing temperature. Each firing temperature contains at least 5 wafers. Their parameters were shown in Table D-1 and D-2.

Table D- 1 Cell efficiency of commercially available silver paste without CNF

Target peak Temperature : 790°C, ramp-up rate : 100°C/s															
wafer no.	Peak firing Temperature (°C)	Ramp-up rate (°C/s)	average finger line width (μm)	V _{oc} (mV)	I _{sc} (A)	J _{sc} (mA/cm ²)	FF (%)	pFF (%)	Pm (W)	Vm (V)	Im (A)	EFF (%)	pEFF (%)	R _s (mΩ)	R _{sh} (Ω)
1	784	97.93	59.996	634	8.621	36.07	79.0	83.0	4.321	0.539	8.018	18.1	18.9	6	8.55
3	791	100.34	61.538	633	8.480	35.48	80.7	82.6	4.335	0.545	7.954	18.1	18.5	7	17.82
7	789	99.66	68.45	635	8.539	35.73	80.2	83.0	4.348	0.546	7.965	18.2	18.7	6	10.21
10	781	96.9	87.518	635	8.401	35.15	80.6	83.2	4.300	0.546	7.876	18.0	18.5	7	13.05
13	792	100.89	75.952	635	8.460	35.40	80.5	83.2	4.329	0.546	7.930	18.1	18.6	6	38.13
Target peak Temperature : 810°C, ramp-up rate : 100°C/s															
wafer no.	Peak firing Temperature (°C)	Ramp-up rate (°C/s)	average finger line width (μm)	V _{oc} (mV)	I _{sc} (A)	J _{sc} (mA/cm ²)	FF (%)	pFF (%)	Pm (W)	Vm (V)	Im (A)	EFF (%)	pEFF (%)	R _s (mΩ)	R _{sh} (Ω)
4	815	101.61	63.096	636	8.475	35.46	80.7	82.9	4.353	0.552	7.887	18.2	18.6	6	12.07
5	808	99.35	69.76	636	8.535	35.71	80.1	82.7	4.347	0.552	7.876	18.2	18.7	6	6.11
8	815	101.61	74.76	635	8.513	35.62	80.5	82.7	4.350	0.552	7.882	18.2	18.6	6	6.14
11	816	101.94	70.478	635	8.434	35.29	80.6	83.0	4.320	0.546	7.914	18.1	18.5	6	38.39
17	809	99.68	60.95	636	8.614	36.04	79.3	82.7	4.339	0.541	8.021	18.2	18.6	6	6.15
Target peak Temperature : 830°C, ramp-up rate : 100°C/s															
wafer no.	Peak firing Temperature (°C)	Ramp-up rate (°C/s)	average finger line width (μm)	V _{oc} (mV)	I _{sc} (A)	J _{sc} (mA/cm ²)	FF (%)	pFF (%)	Pm (W)	Vm (V)	Im (A)	EFF (%)	pEFF (%)	R _s (mΩ)	R _{sh} (Ω)
2	827	99.09	61.194	635	8.616	36.05	80.6	82.7	4.408	0.552	7.987	18.4	18.9	6	3.39
6	826	98.79	73.334	634	8.357	34.97	79.9	82.9	4.234	0.539	7.857	17.7	18.3	6	8.91
9	826	98.79	73.334	634	8.357	34.97	79.9	82.9	4.234	0.539	7.857	17.7	18.3	6	8.91
12	816	95.75	72.734	636	8.467	35.43	78.4	83.0	4.220	0.540	7.817	17.7	18.6	7	4.14
15	822	97.56	72.734	636	8.467	35.43	78.4	83.0	4.220	0.540	7.817	17.7	18.6	7	4.14
14	823	104.19	73.334	635	8.430	35.27	80.2	83.0	4.298	0.540	7.960	18.0	18.5	6	8.19
18	825	104.84	62.38	635	8.626	36.09	77.9	82.7	4.265	0.535	7.973	17.8	18.6	8	18.57

Table D- 2 Cell efficiency of commercially available silver paste containing 0.2 wt% CNF

Target peak Temperature : 790°C, ramp-up rate : 100°C/s															
wafer no.	Peak fining Temperature (°C)	Ramp-up rate (°C/s)	average finger line width (μm)	V _{oc} (mV)	I _{sc} (A)	J _{sc} (mA/cm ²)	FF (%)	pFF (%)	Pm (W)	Vm (V)	Im (A)	EIT (%)	pEIT (%)	R _s (mΩ)	R _{sh} (Ω)
2	791	100.34	46.806	635	8.583	35.91	80.6	83.1	4.395	0.552	7.963	18.4	18.9	6	449.80
4	789	99.66	48.096	637	8.679	36.32	80.1	82.9	4.425	0.547	8.091	18.5	19.1	6	6.52
8	792	100.69	48.816	638	8.567	35.85	80.6	83.1	4.408	0.542	8.135	18.4	18.9	6	6.32
10	790	100	48.096	637	8.617	36.06	80.4	82.9	4.417	0.553	7.988	18.5	18.9	6	6.72
15	782	97.24	45.95	634	8.623	36.08	78.8	82.9	4.313	0.535	8.062	18.0	18.9	7	13.35
16	792	100.69	46.38	635	8.623	36.08	78.9	82.9	4.318	0.535	8.072	18.1	18.9	7	11.85
Target peak Temperature : 810°C, ramp-up rate : 100°C/s															
wafer no.	Peak fining Temperature (°C)	Ramp-up rate (°C/s)	average finger line width (μm)	V _{oc} (mV)	I _{sc} (A)	J _{sc} (mA/cm ²)	FF (%)	pFF (%)	Pm (W)	Vm (V)	Im (A)	EIT (%)	pEIT (%)	R _s (mΩ)	R _{sh} (Ω)
1	814	101.29	45.24	638	8.603	36.00	79.1	83.1	4.341	0.541	8.025	18.2	19.0	7	14.50
5	813	100.96	48.81	634	8.568	35.85	80.4	82.8	4.370	0.551	7.933	18.3	18.8	6	14.23
7	815	101.61	49.246	637	8.615	36.05	80.2	83.1	4.403	0.553	7.964	18.4	19.0	6	8.96
12	804	98.06	48.602	637	8.599	35.90	80.7	82.9	4.418	0.553	7.990	18.5	18.9	6	7.59
14	815	101.61	48.81	636	8.619	36.06	80.8	83.2	4.425	0.546	8.105	18.5	18.9	6	21.26
19	815	101.61	45.16	632	8.553	35.79	78.5	82.9	4.248	0.533	7.971	17.8	18.9	7	160.56
Target peak Temperature : 830°C, ramp-up rate : 100°C/s															
wafer no.	Peak fining Temperature (°C)	Ramp-up rate (°C/s)	average finger line width (μm)	V _{oc} (mV)	I _{sc} (A)	J _{sc} (mA/cm ²)	FF (%)	pFF (%)	Pm (W)	Vm (V)	Im (A)	EIT (%)	pEIT (%)	R _s (mΩ)	R _{sh} (Ω)
3	831	100.3	49.462	637	8.593	35.95	79.1	83.1	4.326	0.535	8.087	18.1	18.9	6	6.54
6	830	100	47.97	636	8.561	35.82	78.2	83.0	4.259	0.540	7.888	17.8	18.8	7	4.80
9	829	99.7	48.548	637	8.572	35.87	79.9	83.0	4.363	0.547	7.978	18.3	18.8	6	7.38
13	824	101.25	48.572	635	8.565	35.84	80.9	83.1	4.398	0.546	8.057	18.4	18.8	6	18.70
18	838	105.625	46.67	633	8.613	36.04	79.3	82.9	4.325	0.539	8.025	18.1	18.9	7	7.26

Appendix E

Sheet resistance, shunt resistance and I-V curve

When the equivalent circuit of a solar cell is considered, two important resistances in solar cell fabrication can be seen as Fig. E-1. One is shunt resistance (R_{sh}) which caused by the leakage across the junctions around the edge of the cell and the manufacturing defects. Another is series resistance (R_s) which caused by the bulk resistance of semiconductor materials. The bulk resistance includes the resistance of the metallic contacts, interconnections and the contact between the metal electrode and the semiconductor. In order to minimize the loss in solar cell, the shunt resistance should to be as high as possible and series resistance should to be as low as possible. High series resistance effects on the reduction of the output voltage, resulting in lower FF. A low shunt resistance effects on leaking of some current and also lowers the FF [84].

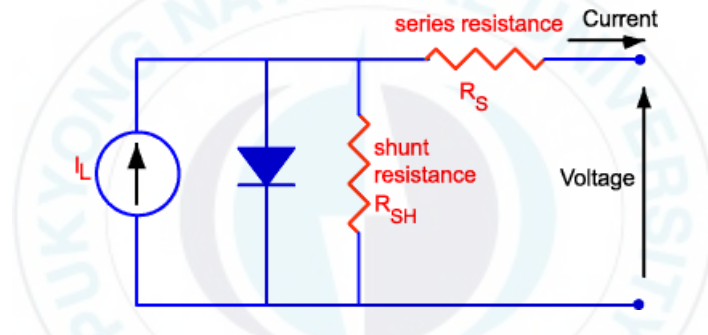


Fig. E-1 The equivalent circuit model [85]

Although there are a variety of methods to estimate R_{sh} and R_s , one of the most straightforward techniques is to measure the slope of IV characteristics as shown in Fig. E-2. R_{sh} and R_s is represented by the slope at I_{sc} and V_{oc} , respectively [86, 87].

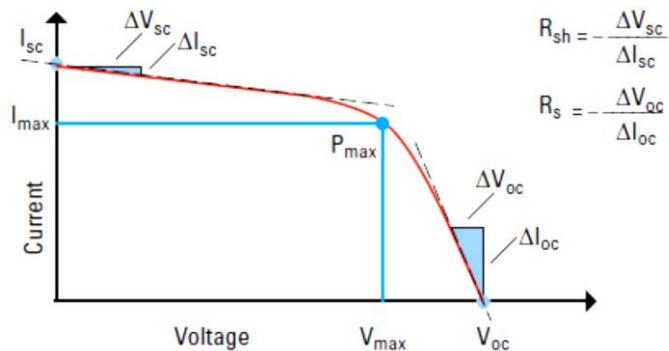


Fig. E-2 Obtaining values for R_s and R_{sh} from I-V curve [86]

Superimposition of IV characteristic of cells prepared by commercially available silver paste without CNF is obtained with cells prepared by commercially available silver paste with 0.2 wt% CNF at different peak firing temperature. The Origin software is used in the operation of the curves enables a sample fitting direct access to the slope (shunt resistance) on the previous described zones. This method allows to accurately the value of shunt resistance without using the equation.

As shown in Fig. E-3 to Fig. E-6, the incorporation of CNF in commercially available silver paste not only improved the shunting problem because of the CNF prevented the aggressive glass frit to etch away SiN_x and emitter layer but also improved the J_{sc} due to the substantially shading losses. However there is no difference between R_s of both cells. The results obtained are summarized in Table E-1.

Table E-1 Summary of shunt resistance from I-V curves.

CNF concentration (wt%)	Peak firing temperature ($^{\circ}\text{C}$)	Slope at I_{sc}	$-(1/\text{slope})$	Shunt resistance (Ω)
0	790	-0.228	4.39	4.39
0.2	790	-0.140	7.14	7.14
0	810	-0.148	6.76	6.76
0.2	810	-0.133	7.52	7.52
0	830	-0.233	4.29	4.29
0.2	830	-0.163	6.13	6.13

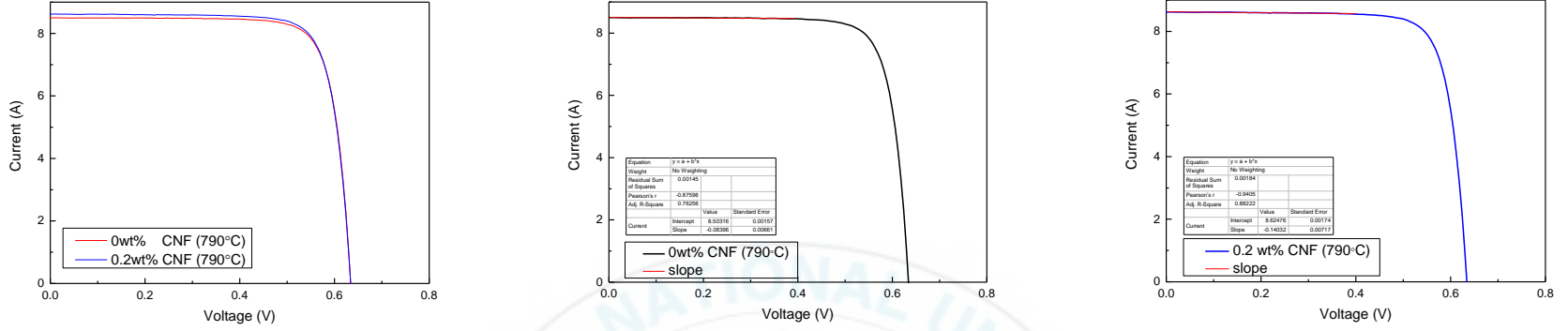


Fig. E-3 I-V curve of cells prepared by commercially available silver paste without and with 0.2 wt% CNF at peak temperature of 790°C

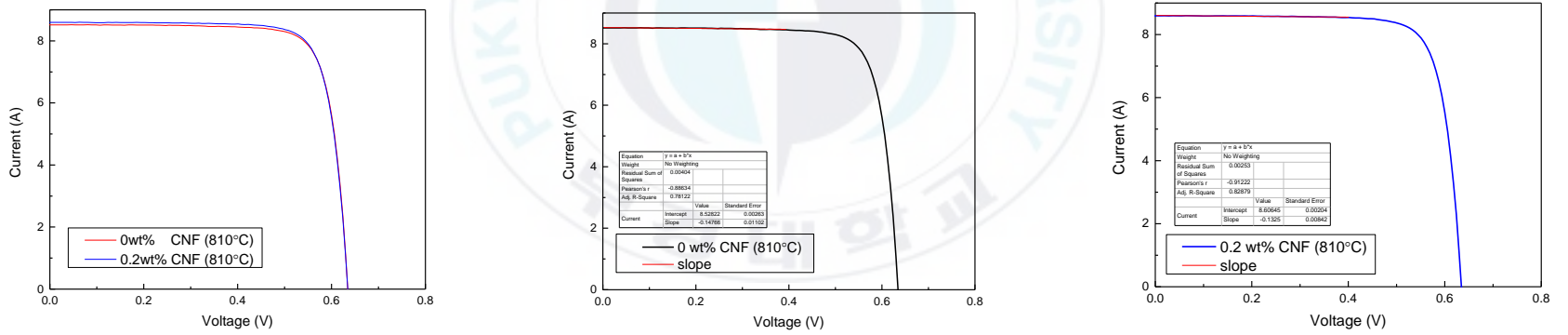


Fig. E-4 I-V curve of cells prepared by commercially available silver paste without and with 0.2 wt% CNF at peak temperature of 810°C

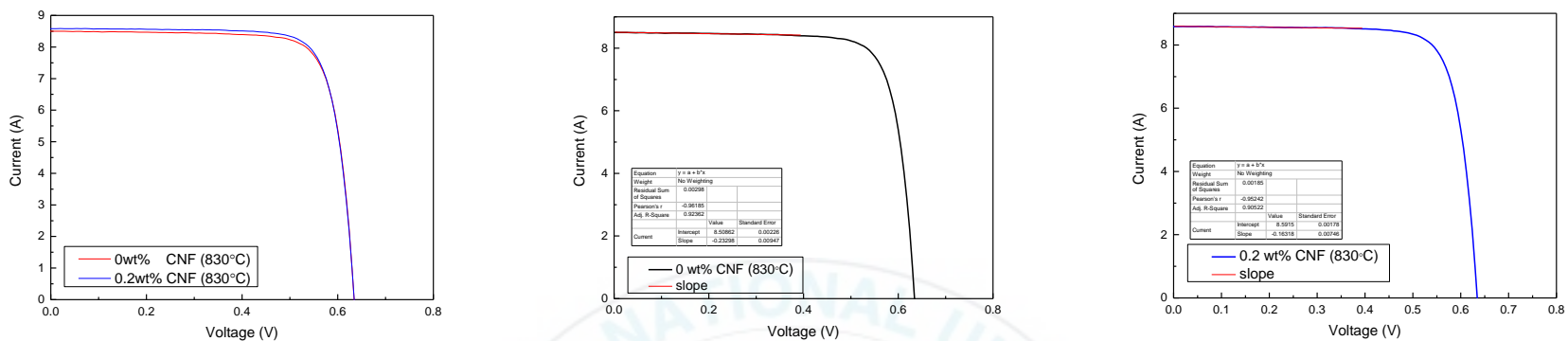


Fig. E-5 I-V curve of cells prepared by commercially available silver paste without and with 0.2 wt% CNF at peak temperature of 830°C

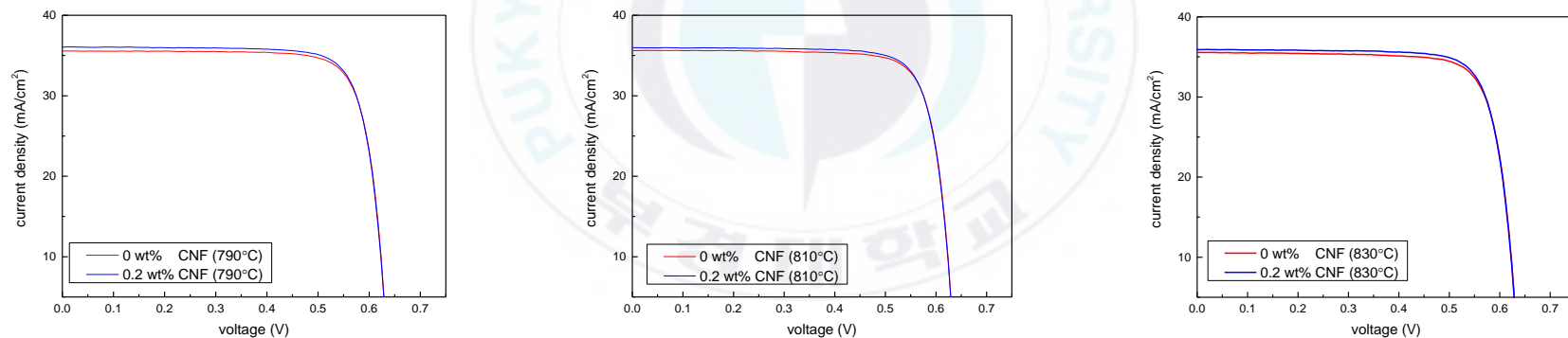


Fig. E-6 J-V curve of cells prepared by commercially available silver paste without and with 0.2 wt% CNF at peak temperature of 790, 810 and 830°C

6. Reference

- [1] U.S Energy Information Administration, 2013. Today in energy. Retrieved 19 January, 2016, from <http://www.eia.gov/todayinenergy/detail.cfm?id=12251>
- [2] SEMI P.V. Group 2015, International Technology Roadmap for Photovoltaic (ITRPV.net), Results 2015.
- [3] L. Zhongtian., C. Ran., Y. Yu., Z. Wei., W. Xi., P.W. Ivan., & L. Alison. (2014). Patterning and Metallization of Silicon Solar Cells by Inkjet-Printed Functional Ink on a Photoresist Layer. *IEEE*, 2499-2501.
- [4] L. Baochen., G.A. Armin., M. Thomas., K.V. Lalit., J.D. Aaron., Y. Hyunsoo., & S.B. Charanjit. (2012). Ultrafine and High Aspect Ratio Metal Lines by Electron Beam Lithography for Silicon Solar Cell Metallisation. *Energy Procedia*, 15, 91-96.
- [5] Glunz, S. W. (2007). High-Efficiency Crystalline Silicon Solar Cells. *Advances in OptoElectronics*. doi: 10.1155/2007/97370
- [6] L. Baochen., G. A. Armin., M. Thomas., K. V. Lalit., J. D. Aaron., Y. Hyunsoo., & S.B. Charanjit. (2012). Ultrafine and High Aspect Ratio Metal Lines by Electron Beam Lithography for Silicon Solar Cell Metallisation. *Energy Procedia*, 15, 91-96.
- [7] Henderson, C. L. Microlithography. Retrieved 30 December, 2015, from <http://henderson.chbe.gatech.edu/Introductions/microlithography%20intro.htm>
- [8] M. Beutel., A. Lewis., M. Prondzinski., F. Selbmann., P. Richter., F. Bamberg., P. Raschtschepkin., A. Krause., C. Koch., M. Hentsche., K.H. Stegemanna., E. Schneiderlöchner., & H. Neuhaus (2014). Fine line metallization by coextrusion technology for next generation solar cells. *Solar Energy Materials & Solar Cells*, 113, 64-71.
- [9] L.P. Richter., F. Gerd., S. Lamine., H. Melanie., S. Stefan., M. Matthias., L.C. Corie., E.S. Scott., R. Ranjeet., E. Scott., P. Phedon., S. Eric., & D.H. Neuhaus (2015). Progress in fine-line metallization by co-extrusion printing on cast monosilicon PERC solar cells. *Solar Energy Materials & Solar Cells*, 142, 18-23.
- [10] M. Ju., Y. J. Lee., J. H. Lee., B. Kim., K. Ryu., K. Choi., K. Song., K. Lee., C. Han., Y. Jo., & J. Yi. (2012). Double screen printed metallization of crystalline silicon solar cells as low as 30 nm metal line width for mass production. *Solar Energy Materials and Solar cells*, 100, 204-208.
- [11] L. D. Dobrzański., M. Muszyfaga., & A. Drygała. (2013). Final Manufacturing Process of Front Side Metallisation on Silicon Solar Cells Using Conventional and Unconventional Techniques. *Mechanical Engineering*, 59, 175-182.
- [12] T. Ignacio., C. Carlosdel., & A. Jes'us (2003). Crystalline Silicon Solar Cells and Modules. In A. Luque & S. Hegedus (Ed.), *Handbook of Photovoltaic Science and Engineering*.: John Wiley & Sons, Ltd.
- [13] M. Pospischil., M. K., M. Kuchler., J. Specht., H. Gentischer., R. Efinger., C. Kroner., M. Luegmair., M. König., M. Hörteis., C. Mohr., L. Wende., J. Lossen., M. Weiß., O. Doll., I. Koehler., R. Zengerle., F. Clement., & D. Biro. (2015). Dispensing Technology on the Route to an Industrial Metallization Process. *Energy Procedia*, 67, 138-146.

- [14] D.H. Kim., S. S. Ryu., D.W. Shin., J.H. Shin., J.J. Jeong., H.J. Kim., & H.S. Chang. (2012). The fabrication of front electrodes of Si solar cell by dispensing printing. *Materials Science and Engineering B*, 177, 217–222.
- [15] Martins, J. (2013). *Design and Fabrication by Inkjet Printing of Electrodes for Electromyography*. University of Lisboa.
- [16] D. M. Graham., D. H. S., & M. H. Ian. (2008). Inkjet printing- the physics of manipulating liquid jets and drops. *Physics*, 105, 012001.
- [17] D. Y. Shin., Y. K. Cha., H. H. Ryu., S. H. Kim. (2012). Impact of effective volume ratio of a dispersant to silver nano-particles on silicon solar cell efficiency in direct ink-jet metallization. *Micromechanics and Microengineering*, 22, 115007.
- [18] K.F. Teng., & R. W. Vest. (1988). Application of Ink Jet Technology on Photovoltaic Metallization. *IEEE Electron Device Letters*, 9, 591-593.
- [19] Y. Satarou., U. Atsushi., A. Yoko., M. Keisuke. (2013). Piezoelectric inkjet-based one cell per one droplet automatic printing by image processing. *IEEE*, 502 - 507.
- [20] K. F. Teng., & R. W. Vest. (1988). Metallization of Solar Cell with Ink Jet Printing and Silver Metallo-Organic Inks *IEEE Transactions on Components, Hybrids, and Manufacturing Technology*, 11, 291-297.
- [21] Y Y.T. Gizachew., L. E., J.J.Simon., M. Pasquinelli., J. Loiret., P.Y. Leguen., J.C.J imeno., J. Martin., A. Apraiz., & J.P. Aguerre. (2011). Towards ink-jet printed fine line front side metallization of crystalline silicon solar cells. *Solar Energy Materials and Solar cells*, 96, 570-583.
- [22] M. Ankit., C. F. D., & F. F. Lorraine. (2013). Optimization of Aerosol Jet Printing for High-Resolution, High- Aspect Ratio Silver Lines. *ACS Applied Materials & Interfaces*, 5, 4856–4864.
- [23] A. Mette., P. L. Richter., M. Horteis., & S. W. Glunz. (2007). Metal Aerosol Jet Printing for Solar Cell Metallization. *Prog. Photovolt*, 15, 621-627.
- [24] B. Sebastian., S. Christian., G. Markus., & W.G. Stefan. (2014). *Optimize Aerosol Printed Silver contacts on lowly doped phosphorus and boron emitters*. Paper presented at the 29th European PV Solar Energy Conference and Exhibition, Amsterdam, The Netherlands.
- [25] M. Hörteis. (2008). Aerosol-Printed Silicon Solar Cell Exceeding 20% Efficiency. Crystal-Clear-Workshop, Metallization, Fraunhofer Institute Solare Energiesysteme.
- [26] D. Y. Shin., S. S. Yoo., S. Hee-eun., T. Hyowon., & B. Doyoung (2015). Electrostatic-Force-Assisted Dispensing Printing to Construct High-Aspect-Ratio of 0.79 Electrodes on a Textured Surface with Improved Adhesion and Contact Resistivity. *Scientific Reports*. doi: 10.1038/srep16704
- [27] Glunz, S. W. (2007). High-Efficiency Crystalline Silicon Solar Cells. *Advances in OptoElectronics*. doi: 10.1155/2007/97370
- [28] M. Pospischila., M. Kuchler., M. Klawitter., C. Rodriguez., A. Padilla., R. Efinger., H. Gentscher., M. König., M. Hörteis., L. Wende., O. Doll., F. Clement., & D. Biro. (2014). *Ultrafine front side metallization on silicon solar cell by industrial dispensing technology*. Paper presented at the 29th European PV solar cell conference and exhibition, Amsterdam, The Netherlands.

- [29] H. Helge., D. Thorsten., F. Tom., & B. Rolf. (2103). Fineline printing options for high efficiencies and low Ag paste consumption. *Energy Procedia*, 38, 725 – 731.
- [30] M. Pospischil. K. Zengerle., J. S., G. Birkle., P. Koltay., R. Zengerle., & A. Henning., M. N., C. Mohr., F. Clement., & D. Biroa. (2011). Investigations of Thick-Film-Paste Rheology for Dispensing Applications. *Energy Procedia*, 8, 449-454.
- [31] M. Pospischil., M. K., M. Kuchler., J. Specht., H. Gentischer., R. Efinger., C. Kroner., M. Luegmair., M. König., M. Hörteis., C. Mohr., L. Wende., J. Lossen., M. Weiß., O. Doll., I. Koehler., R. Zengerle., F. Clement., & D. Biro. (2014). Optimizing fine line dispensed contact grids. *Energy Procedia*, 55, 693-701.
- [32] M. Pospischil., M. K., M. Kuchler., J. Specht., H. Gentischer., R. Efinger., C. Kroner., M. Luegmair., M. König., M. Hörteis., C. Mohr., L. Wende., J. Lossen., M. Weiß., O. Doll., I. Koehler., R. Zengerle., F. Clement., & D. Biro. (2013). Process Development for a High-Throughput Fine Line Metallization Approach Based on Dispensing Technology. *Energy Procedia*, 43, 111-116.
- [33] Carbon nano-material Technology Co., Ltd. Graphite nanofiber: GNF-L Retrieved 18 January, 2016, from <http://www.carbonnano.co.kr/english/english.htm>
- [34] Pyrograf production, Inc. A Comparison of Carbon Nanotubes and Carbon Nanofibers Retrieved 18 January, 2016, from <http://pyrografproducts.com/carbon-nanotubes.html>
- [35] S. Lan-Hui., O. Z., G. Xin-Lin., A.W. Casey., & Y. Zhen-Guo. (2011). Preparation, Characterization, and Modeling of Carbon Nanofiber/Epoxy Nanocomposite. *Nanomaterials*. doi: 10.1155/2011/307589
- [36] S.L. Chee. (2007). *Mechanical and Electrical properties of aligned Carbon nanofiber/epoxy nanocomposite*. (Bachelor of Science), Wichita State University.
- [37] F. Lichao., X. Ning., & Z. Jing. (2014). Carbon Nanofibers and Their Composites: A Review of Synthesizing, Properties and Applications. *Materials*, 7, 3919-3945.
- [38] M. Endo., Y.A. Kim., T. Hayashi., K. Nishimur., T. Matusit., & K. Miyashit. (2001). Vapor-grown carbon fibers (VGCFs) Basic properties and their battery applications. *Carbon*, 39, 1287–1297.
- [39] O. Tanil., N. Mohammad., C. Ioannis. (2010). Mechanical properties of vapor grown carbon nanofiber. *Carbon*, 48, 239–244.
- [40] C. Xi., J. B., C. Boyuan., F. Jia., C. Ze., Z. Xiaodan., Z. Ying., & G. Min (2015). Graphenized Carbon Nanofiber: A Novel Light-Trapping and Conductive Material to Achieve an Efficiency Breakthrough in Silicon Solar Cells. *Advanced Materials*, 27, 849–855.
- [41] H. Matthias., G. Tobias., R. Armin., & W.G. Stefan. (2010). High-Temperature Contact Formation on n-Type Silicon: Basic Reactions and Contact Model for Seed-Layer Contacts. *Advanced Functional Materials*, 20, 476-484.
- [42] P. Jin-Man., P. Keun-Hwan., P. Eun-Soo., H. Seok-Moo., K. Yun-Kim., J. Sand-Soo., L. Eun-Sung., K. Suck-Jun., K. Ki-buem., K. Do-Hyang., & J. ECKERT. (2015). *Effect of Metallic Glass Particle Size on the Contact Resistance of Ag/Metallic Glass Electrode*. Paper presented at the The Minerals, Metals & Materials Society and ASM International 2015.

- [43] C. Quande., Y. Hongxing., L. Lin., & W. Yuanhao. (2013). Preparation of lead-free nanoglass frit powder for crystalline silicon solar cells. *Applied Energy*, 112, 657–662.
- [44] Planetary Micro Mill PULVERISETTE 7 premium line. Retrieved 18 January, 2016, from <http://www.fritsch-milling.com/solutions/grinding>
- [45] K. Kyunghae., K. D. Suresh., G. Utpal., Y. Jinsu., S. Choi-Won., & Y. Junsin. (2006). A novel approach for co-firing optimization in RTP for the fabrication of large area mc-Si solar cell. *Thin Solid Films*, 511, 228 – 234.
- [46] T. Kwon., S. K., D. Kyung., W. Jung., S. Kim., Y. Lee., Y. Kim., K. Jang., S. Jung., M. Shin., & J. Yi. (2010). The effect of firing temperature profiles for the high efficiency of crystalline Si solar cells. *Solar Energy Materials and Solar*, 94, 823-829.
- [47] Contact resistance and TLM measurements. Retrieved 30 December, 2015, from http://tuttle.merc.iastate.edu/ee432/topics/metals/tlm_measurements.pdf
- [48] A. Mary., G. R., & Keithley Instruments, Inc. (2011). Tools and Techniques for Testing Nanotech. Retrieved 18 January, 2016, from <http://www.designworldonline.com/tools-and-techniques-for-testing-nanotech/>
- [49] F. M. Smits. (1958). Measurement of Sheet Resistivity with Four-Point Probe. *The Bell System Technical*, 711-718.
- [50] C. Simona., F. D., T. Daniela & L. M. Pier. (2008). Rheology of carbon nanofiber-reinforced polypropylene. *Rheol Acta*, 47, 425-433.
- [51] O. Yasufumi., F. M., K. Masahiro., & E. Kazuya (2007). Shear-thickening flow of suspensions of carbon nanofibers in aqueous PVA solutions. *Rheol Acta*, 46, 905–912.
- [52] Y. Mohamed., G. D., & L. Bernard. (2015). Suspensions of carbon nanofibers in organic medium: rheo-electrical properties. *Royal Society of Chemistry*, 17, 32316-32327.
- [53] X. Jianhua., C. S., W.K. Kurt., W. Yingru., & E. B. Stephen. (2005). Shear and extensional rheology of carbon nanofiber suspensions. *Rheol Acta*, 44(537-562).
- [54] M.F. Stuckings., & A.W. Blakers (1999). A study of shading and resistive loss from the fingers of encapsulated solar cells. *Solar Energy Materials and Solar cells*, 59, 233-242.
- [55] L. Baochen., A. G. Aberle., M. Thomas., L.K. Verma., A.J. Danner., Y.Hyunsoo., & C.S. Bhatia. (2012). Ultrafine and High Aspect Ratio Metal Lines by Electron Beam Lithography for Silicon Solar Cell Metallisation. *Energy Procedia*, 15, 91-96.
- [56] M. Debasis., T. N. Blanton., & D.W. Schwark. (2003). Clay–polymer nanocomposite coatings for imaging application. *Applied Clay Science*, 23, 265– 273.
- [57] H. Matthias., G. Tobias., R. Armin., & W. Stefan. (2010). High-Temperature Contact Formation on n-Type Silicon: Basic Reactions and Contact Model for Seed-Layer Contacts. *Advanced Functional Materials*, 20, 476-484.

- [58] C. Ballif., D. M. Huljic., G. Willeke., & A. Hessler-Wyser. (2003). Silver thick-film contacts on highly doped n-type silicon emitters: Structural and electronic properties of the interface. *Applied Physics Letters*, 82, 1878-1880.
- [59] Z. G. Li., L. Liang, & L. K. Cheng. (2009). Electron microscopy study of front-side Ag contact in crystalline Si solar cells. *Applied Physics*, 105, 066102.
- [60] C.H. Lin., S. P. Hsu., & W. C. Hsu. Silicon Solar Cells: Structural Properties of Ag-Contacts/Si-Substrate (pp. 93-110): Industrial Technology Research Institute, Taiwan, R.O.C.
- [61] R.J. Wakeman., & E. S. Tarleton. (1999). Filtration: equipment selection, modelling and process simulation: Elsevier Advanced Technology.
- [62] R.J. Wakeman., & E. S. Tarleton. (2005). Solid/liquid separation: principles of industrial filtration: Elsevier Advanced Technology.
- [63] X. Qingrong., J. Claudia., S. Katja., & P.J. Andrey. (2015). Measurement and modeling of reactive transport in geological barriers for nuclear waste containment. Royal Society of Chemistry, 17, 30577-30589.
- [64] L. Kenneth., N. S. (2016). Enhancement mechanism of NCMs on properties of cementitious composites *Innovation Developments of Advanced Multifunctional Nanocomposites in Civil and structural Engineering*: ELSEVER and Woodhead publishing.
- [65] P. N. Vinod. (2011). Specific contact resistance measurements of the screen-printed Ag thick film contacts in the silicon solar cells by three-point probe methodology and TLM method. *J Mater Sci: Mater Electron*, 22, 1248-1257
- [66] K. Christopher., L. B., B. Ulrike & D. Thorsten. (2015). Determination of the contact resistivity of screen-printed Al contacts formed by laser contact opening. *Energy Procedia*, 67, 64-69.
- [67] D. Pysch., A. M., A. Filipovic., & S. W. Glunz. (2009). Comprehensive Analysis of Advanced Solar Cell Contacts Consisting of Printed Fine-line Seed Layers Thickened by Silver Plating. *Progress in photovoltaics: Research and Application*, 17, 101-114.
- [68] Center of Information and Numerical Data Analysis and Synthesis. (1974). Electrical Resistivity of Copper, Gold, Palladium and Silver. *J. Phys. Chem. Ref. Data*, 8, 041147-041199.
- [69] Instruction Manual Heeke viscometer 550. In T. Scientific (Ed.)
- [70] Resources, C. E. L. (2014). Newtonian and non-Newtonian Fluids. Retrieved 12 March, 2016, from <http://www.msubbu.in/ln/fm/Unit-I/NonNewtonian.htm>
- [71] Neutrium. (2012). Viscosity. Retrieved 11 April, 2016, from <https://neutrium.net/fl>
- [72] C. C. Gary., P. M. Robert., V. Roger., & F. Louise. (1984). Thick-Film Metallization for Solar Cell Applications. *IEEE Transaction on Electron Devices*, 31, 602-609.
- [73] C. Bo-Mook., C. S.-B., C. Jung-Woo., K. Young-Sik., O. Kuninori., & H. Joo-Youl. (2013). Influence of oxygen on Ag ionization in molten lead borosilicate glass during screen-printed Ag contact formation for Si solar cells. *Electrochemical Acta*, 106, 333-341.

- [74] S. Kontermann., M. H. r., M. Kasemann., A. Grohe., R. Preu., E. Pink., & T. Trupke. (2009). Physical understanding of the behavior of silver thick-film contacts on n-type silicon under annealing conditions. *Solar Energy Materials & Solar Cells*, 93, 1630-1635.
- [75] M. H. Mohamed., S. S., K. Chandra., S. Aziz., R. Ajeet., & K. Steve. (2006). Effect of Glass Frit Chemistry on the Physical and Electrical Properties of Thick-Film Ag Contacts for Silicon Solar Cells. *Electronic Materials*, 35, 241-247.
- [76] O. N. Hartley., R. R., K.C. Heasman., N.B. Mason., & T.M. Bruton. (2002). Investigation of Thin Aluminium Films on the Rear of Monocrystalline Silicon Solar Sell for Back Surface Field Formation. *IEEE*, 7803-7471.
- [77] B. Sopori., V. M., P. Rupnowski., & H. Moutinho. (2009). *Studies on Backside Al-Contact Formation in Si Solar Cells: Fundamental Mechanisms*. Paper presented at the the Materials Research Society (MRS) Fall Meeting 2008, Boston, Massachusetts.
- [78] K. Vichai., N. K., S. K. Dong., K. Steve., S. Aziz., K. Armin., S. Werner., & R. Ajeet (2006). Investigation of Modified Screen-Printing Al Pastes for Local Back Surace Field Formation. *IEEE*, 1-4244-0016-3.
- [79] E. Ryabova., A. S., I. J. Malik., & M. Shkolnikov. (2010). Novel Back Surface Field (BSF) Structure Formation by Modified Solution Derived Nanocomposite (SCN) Method for Low Cost New Cell Concept Implementation. *IEEE*, 978-971-4244-5892-4249.
- [80] N. Shreesh., R. A., & A. W. Weeber. (1999). An Optimized Rapid Aluminum Back Surface Field Technique for Silicon Solar Cells. *IEEE Transactions on Electron Device*, 46, 1363-1370.
- [81] D.L. Bätzner., K. H., A. Li., & A. Cuevas. (2006). *Investigation of The Co-firing Process for Contact Formation Screen Printed Silicon Solar Cells*. Paper presented at the 21st European Photovoltaic Solar Energy Conference, Dresden, Germany.
- [82] Haldor, T. (1968). Geometric factors in four point resistivity measurement. *Semiconductor Division*, 472-13.
- [83] MDC. Resistivity Theory. Retrieved 6 January, 2016, from http://www.mdc-europe.com/pdf/Downloads/Resistivity_Theory.pdf
- [84] Niasse, O. A., Tankari, M.A., Dia, F., Mbengue, N., Diao, A., Niane, M., Diagne, M., Ba, B. & Levebvre, G. (2016). Optimization of Electric Parameters CdS/CdTe Thin Film Solar Cell Using Dielectric Model. *World Journal of Condensed Matter Physics*, 6, 75-86.
- [85] PV Education.org. Impact of Both Series and Shunt Resistance. Retrieved 30 May, 2016, from <http://www.pveducation.org/pvcdrom/solar-cell-operation/impact-of-both-resistances>
- [86] Agilent Technologies. (2009). IV and CV Characterizations of Solar/ Photovoltaic Cells Using the B1500A. Retrieved 30 May, 2016, from <http://www.ccontrols.ch/cms/upload/applikationen/Solar-Cell/5990-4428EN.pdf>
- [87] A. R. Burgers., J. A. E., A. Schonecker., & W. C. Sinke. (1996). *Improved Treatment of the Strongly Varying Slope in Fitting Solar Cell I-V Curves* Paper presented at the 25th PVSC, Washington, D.C., U.S.A